Multiscale investigation of calcined clays for stabilisation of natural clays

Canadian Geotechnical Journal

OPEN ACCESS | Research Article

Multiscale investigation of calcined clays for stabilisation of natural clays

Vijayshree Sadasivan[a], **Angela Casarella**[b], **Arezou Baba Ahmadi**[a], **Olga Stamati**[c], **Julie Villanova**[d], **and Jelke Dijkstra**[a]

[a]Chalmers University of Technology, Department of Architecture and Civil Engineering, Gothenburg SE-41296, Sweden; [b]Department of Civil and Environmental Engineering, Imperial College London, London SW7 2AZ, England; [c]Univ. Grenoble Alpes, CNRS, Grenoble INP, 3SR, Grenoble 38000, France; [d]ESRF - The European Synchrotron, Grenoble 38043, France

Corresponding author: **Vijayshree Sadasivan** (email: vijsad@chalmers.se)

Abstract

Recently, calcined clays have emerged as a viable supplementary cementitious material (SCM) in structural concrete. In contrast, less knowledge exists on the use of clay-based SCM as a binder for the stabilisation of natural clays. This study investigates the partial replacement of conventional binders, i.e. ordinary Portland cement (CEM I) and lime, with calcined kaolinites for stabilising a natural sensitive clay, aiming to achieve mechanical strength and microstructural evolution comparable to a traditional lime–cement mix (50:50). A holistic approach is adopted to investigate properties across length scales using electrochemical impedance spectroscopy, miniature cone penetration tests, and synchrotron-based X-ray phase-contrast nano-holo-tomography (nano-CT). The results indicate that mixes with up to 20% replacement of conventional binders with calcined clay exhibit comparable strength and material properties to traditional lime–cement stabilised samples, while offering potential reductions in CO_2 emissions. The findings further indicate that pore water availability is a key factor influencing hydration and the resulting mechanical properties in binder-mixed clays. This availability depends on the proportions of lime, cement, and calcined clay added relative to the natural water content, with cement having the strongest influence on water demand. Consequently, the binder composition in stabilisation of soft clays can be optimised to achieve enhanced performance by considering the water retention characteristics and reactivity of the components in the mix, ultimately leading to improved mechanical strength.

Key words: calcined clays, dry deep mixing, lime cement columns, strength

Résumé

Récemment, les argiles calcinées sont apparues comme un matériau cimentaire supplémentaire (MCS) viable dans le béton structurel. En revanche, on en sait moins sur l'utilisation des MCS à base d'argile comme liant pour la stabilisation des argiles naturelles. Cette étude examine le remplacement partiel des liants conventionnels, c'est-à-dire le ciment Portland ordinaire (CEM I) et la chaux, par des kaolinites calcinées pour stabiliser une argile naturelle sensible, dans le but d'obtenir une résistance mécanique et une évolution microstructurale comparables à celles d'un mélange chaux-ciment traditionnel (50:50). Une approche holistique est adoptée pour étudier les propriétés à différentes échelles à l'aide de la spectroscopie d'impédance électrochimique (SIE), d'essais de pénétration au cône miniature (mCPT) et de la nano-holo-tomographie par contraste de phase à rayons X basée sur le synchrotron (nano-CT). Les résultats indiquent que les mélanges avec un remplacement allant jusqu'à 20 % des liants conventionnels par de l'argile calcinée présentent une résistance et des propriétés matérielles comparables à celles des échantillons stabilisés à la chaux et au ciment traditionnels, tout en offrant des réductions potentielles des émissions de CO_2. Les résultats indiquent en outre que la disponibilité de l'eau interstitielle est un facteur clé influençant l'hydratation et les propriétés mécaniques résultantes dans les argiles mélangées à des liants. Cette disponibilité dépend des proportions de chaux, de ciment et d'argile calcinée ajoutées par rapport à la teneur en eau naturelle, le ciment ayant la plus forte influence sur la demande en eau. Par conséquent, la composition du liant dans la stabilisation des argiles molles peut être optimisée pour obtenir une performance accrue en tenant compte des caractéristiques de rétention d'eau et de la réactivité des composants du mélange, ce qui conduit finalement à une amélioration de la résistance mécanique.

Mots-clés : argiles calcinées, mélange profond à sec, colonnes chaux-ciment, résistance

1. Introduction

Soft natural clays with high water content and low strength present significant challenges for construction and infrastructure development. The strength and stiffness of these clays are commonly improved using methods that mix dry cement-based binders with existing soil. This method, used extensively in the Nordic countries, is referred to as dry deep soil mixing (DDSM). In addition to cement (typically ordinary Portland cement, CEM I), the binders typically include slaked or unslaked lime, to further improve the properties of the stabilised soil with time (Moseley and Kirsch 2004; Topolnicki 2004).

DDSM offers notable advantages over conventional piling methods, in terms of reduced costs, reduced material usage, and improved site reusability (Egan and Slocombe 2010). Despite these advantages, the binders used in DDSM, i.e. cement (CEM I) and lime, contribute approximately 824 g CO_2/ kg and 987 g CO_2/ kg of emissions, respectively (Schorcht et al. 2013; Turner and Collins 2013; Scrivener et al. 2018; Olsson et al. 2023), accounting for about 8% (Andrew 2019) and 1% (Simoni et al. 2022) of global anthropogenic CO_2 emissions. Partial replacement of lime ($Ca(OH)_2$) and cement in the binders with supplementary cementitious materials (SCM) has the potential to significantly reduce CO_2 emissions, with reported reductions depending on the type and proportion of SCM used (e.g., Plusquellec et al. 2021).

Alkali activated cementitious materials such as fly ash and ground granulated blast furnace slag have been studied extensively for use in ground improvement (Arulrajah et al. 2018; Behnood 2018). These binders have been shown to significantly improve mechanical performance compared to soils stabilised with CEM I, while also reducing CO_2 emissions considerably depending on the activator system and replacement levels (Sargent et al. 2013, 2016; Yi et al. 2015; Núñez et al. 2025). Despite achieving promising results, fly ash and slag might become unavailable in the long term (Snellings et al. 2023). This brings focus on new and emerging sustainable cementitious materials (SCMs).

SCMs include natural pozzolans (e.g., volcanic ash and pumice), calcined clays, recycled construction materials (e.g., waste concrete fines and brick powder), and energy-derived ashes such as biomass ash (Snellings et al. 2023). Appropriate refining and processing are required to achieve the required activation by thermal, mechanical, or chemical treatments, where the type and extent of processing are governed by the nature of the source material.

Calcined clays are of particular interest due to their wide availability and their potential to provide controlled and relatively consistent reactivity compared to other emerging SCMs. The activated clay in the binder provides the silica and alumina-rich phases necessary to react under wet and alkaline conditions created by the water in the pores of the natural soil (Jaskulski et al. 2020). Potentially, the natural clay excavated at the building site can be activated for use as SCM in another part of the project. However, such clays are heterogeneous with mixed minerals and nonactive silt particles (diameter above 2 μm). Consequently, their activation requires an appropriate combination of thermal and mechanochemical processing tailored to the mineralogical composition (Fernandez et al. 2011; Hazarika et al. 2024).

In this context, limestone calcined clay cement (LC^3) has emerged as a promising SCM for soil stabilisation in road and pavement construction, due to its improved sustainability and performance (Muchui Mugambi et al. 2024). Building on this, the present study evaluates the performance of calcined clay-based SCMs for stabilising natural clays, using thermally activated 1:1 clay (kaolin) in combination with CEM I and hydrated lime ($Ca(OH)_2$). Calcination of kaolinite clay at temperatures typically between 700 and 950 °C requires lower theoretical heat than the production of clinker for Portland cement, with reductions of up to 36% reported in the literature (Hanein et al. 2021).

The geotechnical performance of stabilised natural clays has been studied at laboratory and field scales (decimetre-metre), with a focus on the mechanical response (e.g., Locat et al. 1990; Boardman et al. 2001; Åhnberg et al. 2003; Löfroth 2005; Larsson et al. 2005*a*, 2005*b*; Xie et al. 2012; Consoli et al. 2020; Paniagua et al. 2022; Ramírez and Korkiala-Tanttu 2023; Wong et al. 2024). One such study demonstrated that a comprehensive understanding of stabilised soils benefits from a multiscale experimental approach, combining mechanical testing with material-scale characterisation (Jiang et al. 2016). For this reason, mechanical tests on stabilised clays are often complemented with postmortem observations on the material scale (μm) using scanning electron microscopy (SEM) to characterise the morphology of the phases (Cong et al. 2014; Ahmed 2015; Sekhar and Nayak 2019; Estabragh et al. 2022). The difficulties in the sample preparation method, however, limits the use of SEM (Korpa and Trettin 2006; Deirieh et al. 2018). Techniques such as X-ray diffraction (XRD), energy-dispersive X-ray spectroscopy, and Fourier-transform infrared spectroscopy are also widely used to characterise the mineralogical and chemical composition of binder mixed clays (Latifi et al. 2015; Nunez et al. 2024).

Alternatively, conductivity measurements can be used to monitor microstructural changes in cementitious systems (Levita et al. 2000; McCarter et al. 2003; Tironi et al. 2013; Huang et al. 2022). Electrochemical impedance spectroscopy (EIS) is a logical extension of classical conductivity measurements and has been successfully used to monitor the hydration of cementitious materials and the evolving microstructure over time. For cement pastes, the use of EIS has been established to study the evolution of the pore structure during curing over time in a nondestructive manner (Christensen et al. 1994). Several models have been proposed to map the electrical and physico-chemical response in cementitious materials (e.g., Song 2000; Mason et al. 2002). However, EIS has not yet been used for natural and calcined clay-based composites.

X-ray nano computed tomography (nano-CT) instruments at 4th generation synchrotron sources enable the submicrometre spatial resolution (0.1–300 μm attaining voxel sizes down to 25 nm (Shirani et al. 2023)) required for the 3D investigation of the microstructures of clay composites and the identification of phases. Unlike some other methods, nano-CT allows for a nondestructive 3D quantification of morpho-

logical differences in various mixes caused by hydration reactions following the addition of binders to the clay.

This work presents a feasibility study on using calcined clays to replace (part of) the binders used in stabilising natural clays, with a focus on linking the material processes at the microscopic scale with the laboratory-scale response. Therefore, an integrated approach for investigating the electrochemical and mechanical properties across scales is developed. EIS and miniature cone penetration tests (mCPT) are used to monitor the curing of different binders mixed with natural clay.

Finally, nano-CT observations are analysed to link the morphological features at the microscale to the emerging engineering properties of different mix designs.

2. Methods

2.1. Electrochemical impedance spectroscopy (EIS)

EIS is a volumetrically averaged measurement that is sensitive to the changes at the material scale (submicrometer), and hence no spatial distribution of the properties is obtained. The electrochemical system formed by the clay mixed with lime, cement, and SCM is excited with an alternating electrical signal (voltage or current). The corresponding current or voltage response is measured over a range of frequencies, from which the complex impedance of the system is determined (e.g., McCarter et al. 1988). Fundamental physical and chemical features at the material scale within the sample are inferred from the real and imaginary parts of the electrical response by fitting an equivalent electrical circuit.

The impedance of the sample is influenced by its dielectric properties, including the permittivity and conductivity that are affected by factors such as the water content of the clay, the ionic conductivity of the pore water, and the constituents of the binder. The impedance, $Z(\omega)$, is a complex quantity expressed as

$$Z(\omega) = Z'(\omega) + jZ''(\omega)$$

where $Z'(\omega)$ is the real part (resistance) and $Z''(\omega)$ is the imaginary part (reactance) of the impedance, and j is an imaginary unit. The real part $Z'(\omega)$ is given by

$$Z'(\omega) = \frac{R}{1 + (\omega RC)^2}$$

The imaginary part $Z''(\omega)$ is given by

$$Z''(\omega) = \frac{\omega R^2 C}{1 + (\omega RC)^2}$$

where R is the resistance, C is the capacitance, and ω is the angular frequency ($\omega = 2\pi f$, with f as the frequency). The real part of the impedance Z' is attributed to the electrical resistance to the flow of current in the sample, while the imaginary part Z'' refers to the change in electrical phase between the excited voltage (or current) and the measured current (or voltage). The change in the electrical phase occurring in the sample results from an electric dipole, such as e.g., the clay platelets, the pore water, and the ions present in the pore water.

The Nyquist plot ($Z' - Z''$) for all frequencies can thus be obtained by fitting an equivalent circuit to evaluate the resistance and capacitance measured in the sample. In this work, the measured electrical response is fitted with an equivalent circuit as recommended by Christensen et al. (1994) (Fig. 1*b*). In this circuit, R_0 represents the offset resistance, while R_2 and the constant phase element (CPE_2) describe the bulk response of the sample, and R_e and the constant phase element (CPE_e) represent the external contributions associated with the measurement setup.

These equivalent circuit elements, in principle, can be directly associated with distinct frequency-dependent processes related to pore solution and hydration-induced microstructural changes. Here, R_0 can be attributed to the electrolyte resistance corresponding to ionic conduction through the pore solution. The parallel combination of R_2 and CPE_2 is attributed to the bulk response of the material, with R_2 reflecting the resistance of the evolving solid–pore microstructure and CPE_2 capturing the nonideal capacitive behaviour arising from microstructural heterogeneity and phase evolution within the material. The second parallel branch, consisting of R_e and CPE_e, represents electrode polarisation effects at the electrode–sample interface, particularly at low frequencies. However, in stabilised clays, such a clear separation is rarely achieved due to the coupled effects of pore-fluid conduction, microstructural evolution, and interfacial polarisation associated with electric dipoles at nanoscale interfaces. Consequently, the bulk response R_S determined from the fitted electrical circuit as $R_s = R_0 + R_2$ is commonly adopted in EIS studies of cement pastes (e.g., Christensen et al. 1994) and is selected here as a representative parameter. This bulk parameter captures the combined effect of the governing mechanisms and allows tracking of hydration progress nondestructively. CPE_2 consists of an arc depression factor n_2, which typically denotes the uniformity in the pore distribution in a sample. When n_2 tends to unity, the CPE_2 demonstrates a pure capacitive behaviour. In cement pastes, this factor is usually 0.7–0.9 (Christensen et al. 1994). In the case of stabilised clays, the pore size distribution is highly complex. Therefore, the parameter n_2 may not be representative for differentiating the pore structure that occurs in different mixes.

2.1.1. EIS test setup

A Metrohm PGSTAT204 potentiostat with a FRA32M EIS board that has a voltage amplitude within a range of +/−10 V and frequency bandwidth of 0.1–1000 000 Hz coupled with Nova 2.1.6 software was used to acquire and process EIS data. A two-electrode configuration was adopted in which the working electrode had five times the surface area of the counter electrode, as suggested by Wang and Xiao (2002). The electrodes were manufactured from printed circuit boards with gold-plated exposed electrodes (Fig. 1*a*). The working electrode was circular, while the counter electrode was spiral

Fig. 1. Electrochemical impedance spectroscopy (EIS) test setup and analysis: (*a*) working electrode (WE) (right) and counter electrode (CE) (left); (*b*) equivalent circuit fitting model (Christensen et al. 1994); (*c*) example of Nyquist plots with fitted equivalent circuit models at 7, 14, 28, 36, and 56 days of curing for mix L80_CC20.

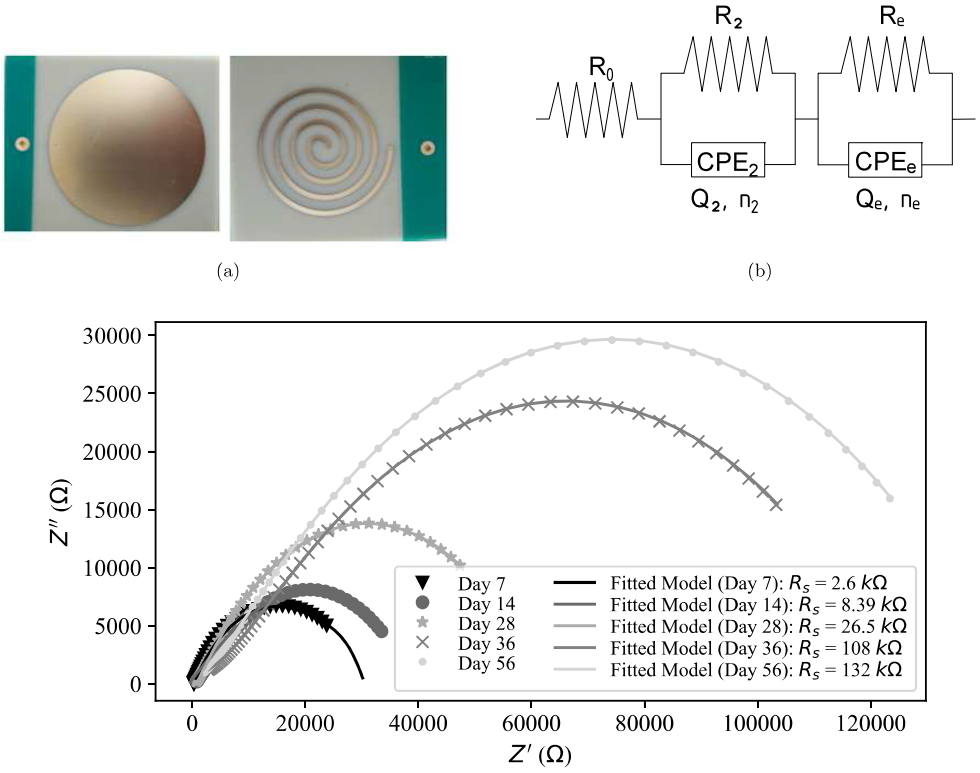

to satisfy the area ratio. During the test, a sinusoidal voltage with an amplitude of 1 V was applied within the frequency range of 0.1–100 000 Hz, and the magnitude and phase change in the electrical current were measured.

The resulting data were fitted with an equivalent circuit as shown in Fig. 1*b*. The quality of the fit had a maximum error of $\chi^2 < 0.2$. The EIS measurement was repeated twice on each sample. Figure 1*c* shows a typical series of Nyquist plots, fitted with an equivalent circuit, for the mix L80_CC20 at 14, 28, 36, and 56 days of curing. The increase in R_s with curing is attributed to the reaction of the binders with the pore water as part of the hydration process, followed by the formation of discontinuous capillary pores (Christensen et al. 1992). Therefore, using this method, the evolution of the different mixes over a period of 56 days could be tracked and compared with the help of the evaluated R_s.

2.2. Miniature cone penetration test (mCPT)

This method is conceptually based on established penetration resistance methods, such as the Proctor needle test in accordance with ASTM C403/C403M-23 (ASTM International 2023), commonly used in concrete testing. The test setup for the miniature penetration tests is shown in Fig. 2. Some components of the Nemesys mid-pressure syringe pump system were used for the actuator. The actuator has a total linear stroke of 60 mm and a minimum constant displacement rate of 60.28 µmmin^{-1}. A stainless steel needle of diameter B = 2 mm with an angle of the cone tip of 60° was used. The penetrations were carried out at a rate of 1 mms^{-1} to a depth of 4 mm, which corresponds to a normalised penetration depth of 2B. Therefore, both the cone resistance and the embedded shaft resistance contribute to the measured penetration resistance. For the small penetration depths considered, the total mechanical resistance is governed by the cone resistance. The total penetration depth was measured using a linear variable differential transformer with a resolution of 0.001 mm. The total penetration resistance was measured at the top of the cone using a load cell with capacity 100 N ± 1 N.

The penetration tests were performed at four points on each side of the sample as seen in section A–A′ of Fig. 2. The scaling laws for physical modelling in geotechnics are adopted to determine the distance between the points (Garnier et al. 2007), since the principle of this test is similar to that of a geotechnical cone penetration test (CPT). The distance from the centre of the cone to the nearest container wall was set to S = 16.7 mm, resulting in a ratio of $S/B \approx 9$. Given the lack of specific guidelines for stabilised clays, this value was selected as an intermediate choice between the commonly used $S/B = 5$ for clays and $S/B = 10$ for coarse-grained soils in standard CPTs. The penetration resistance q_c was calculated as

$$q_c = \frac{F}{A_c}$$

Fig. 2. Front view of the miniature penetration instrument (dimensions in mm).

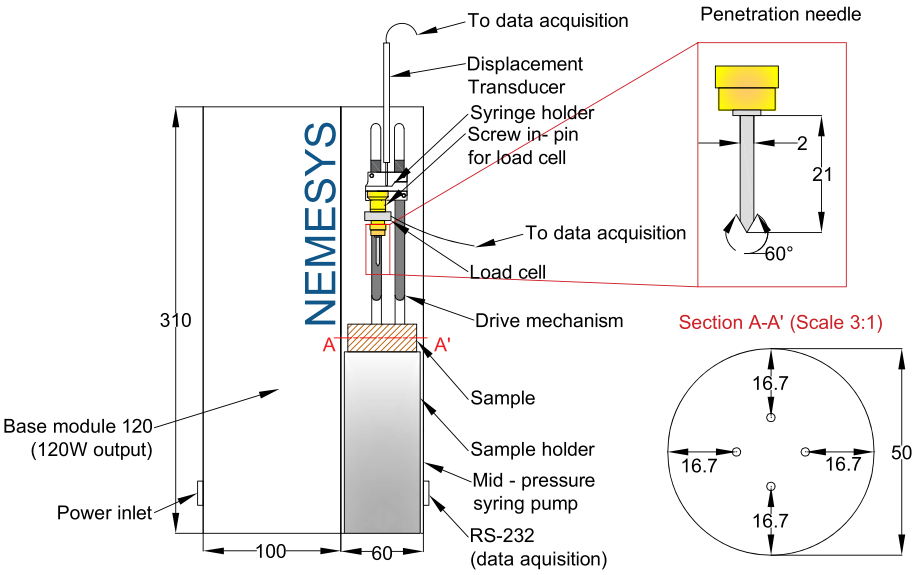

where F denotes the measured force at 4 mm penetration measured by the load cell and A_c denotes the cross-sectional area of the cone B. The peak penetration resistance $q_{c,\,peak}$ for a sample was thus determined as the average resistance at a depth of 4 mm, based on the penetration resistance graph for four points on each side of the sample. A representative result of all individual measurements is shown in Fig. 3. The penetration resistance $q_{c,\,peak}$ exhibits a strong correlation with the compressive strength and, to a lesser extent, with the stiffness of the material, as demonstrated in Appendix A.

2.3. nano-CT

The nano-CT measurements were made at the ID16B beamline of the European Synchrotron Radiation Facility (ESRF) in Grenoble (France) (Martínez-Criado et al. 2016), using the 3D imaging technique of X-ray phase-contrast nano-holotomography (Cloetens et al. 1999). A holo-tomography acquisition consists of combining four tomographic scans taken at different sample-detector distances (changing the propagation distance). This is done to better resolve the phase modulation, ultimately increasing the contrast and spatial resolution in the reconstructed image. The measurements used a beam with an energy of 29.6 keV. During each 360° rotation of the sample, a total of 3023 projections with a pixel size of 25 nm and field of view (FoV) of Φ64 × 54 μm were recorded using a PCO edge 5.5 scientific CMOS camera with an exposure time of 15 ms per projection. The final 3D volumes were obtained after a multistep reconstruction process. First, the individual projections of the four different scans were aligned. Then, the phase retrieval calculation was done using an in-house Octave script (Cloetens et al. 1999) through an iterative calculation based on a Paganin-like approach with δ/β of 150, where δ is the increment of the refractive index and β is the absorption index. Finally, the 3D reconstruction of the retrieved phase maps was performed using a filtered back projection algorithm with ESRF PyHST2 software (Mirone et al. 2014).

2.3.1. Image pre-processing

A central cropped sub-volume of dimensions 1000 × 1000 × 1000 pixels (25 × 25 × 25 μm) of the original reconstructed image was used for the analysis, corresponding to a volume of 15625 μ^3m. This sub-volume was binned using a 2 × 2 × 2 averaging method, yielding a volume of 500 × 500 × 500 pixels. To mitigate noise and reconstruction artefacts, a median 3D filter with a radius of 4 pixels and an unsharp mask filter with 1 pixel pitch and 0.6 weight, were applied using the image processing software ImageJ (Schindelin et al. 2012). Subsequently, the images were normalised with respect to the highest and lowest peaks in the histogram corresponding to the pores and the calcium-rich particles of unmixed cement or lime, respectively.

3. Materials and sample preparation

3.1. Materials

The natural clay used in this study was extracted from the Chalmers soft clay test site in Kärra in Gothenburg City (Sweden), located in the northern part of the city, from a depth of 3–4 m. The natural water content of the clay was determined to be approximately w_n = 80% and the bulk density of the clay in its undisturbed state was determined to be ρ = 1.5 gcm^{-3}. The Atterberg limits and the mineralogy of the clay fraction were determined to be as shown in Table 1. The Kärra clay was composed of 55% clay fraction and 44% silt fraction. The median particle size (D_{50}) of the natural clay was determined to be 1.51 μm using the integral suspension pressure (ISP) method (Durner et al. 2017) with the PARIO particle size analyser (METER Group, Pullman, Washington), following the procedure described by Birmpilis et al. (2022). The calcined clay used in this study was artificially prepared (dry side statically compacted) powder of Speswhite Kaolin clay produced by IMERYS France, activated by heating at a constant temperature of 800 °C for 24 h followed by controlled cooling to 30 °C. Table 1 shows the chemical composition of

Fig. 3. Total penetration resistance q_c measured on the tip of cone as a function of depth for miniature cone penetration tests (mCPT) on 4 points.

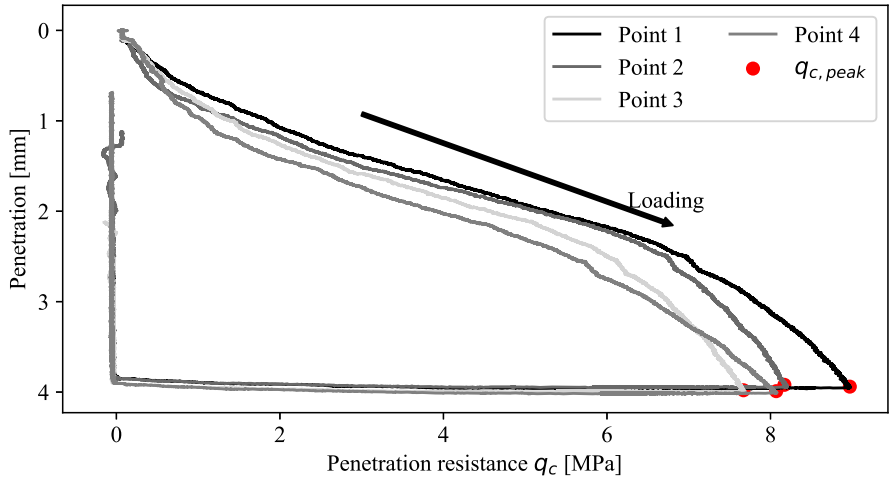

Table 1. Index properties and mineralogical composition of the natural clay.

Kärra clay		
Atterberg limits	Liquid limit, LL (%)	75.6
	Plastic limit, PL (%)	29.5
	Natural water content, w_n (%)	80
Mineralogy of clay fraction (<2 μm) (XRD)	Quartz (%)	20
	Illite (%)	40.7
	Kaolinite (%)	7.2
	Illite/Smectite R0 (14/86) (%)	8.4
	Illite/Smectite R0 (61/39) (%)	36.5
	Chlorite (%)	7.2
Speswhite kaolinite		
Chemical composition (XRF; Casarella 2022)	SiO_2 (%)	46.6
	Al_2O_3 (%)	37.8
	CaO (%)	1.3
	K_2O (%)	2.1
	Loss on ignition LOI (%)	11.3

Note: XRD, X-ray diffraction; XRF, X-ray fluorescence

the Speswhite kaolin clay. The median particle size (D_{50}) of the calcined Speswhite kaolinite was found to range between 3.47 μm (from nano-CT) and 3.79 μm (using ISP method with the PARIO particle size analyser). The ISP tests for the calcined clay were conducted in demineralised water without the addition of chemical dispersants, in order to preserve the flocculated particle structure. Furthermore, CEM I 52.5 R cement supplied by Cementa (Skövde) and 98% lime powder (D_{50}) supplied by Thermo Scientific were used for this study. To adhere to a typical Swedish practice in DDSM (Karlsson and Moritz 2014), the total binder content used throughout this study was maintained at 80 kgm^{-3} which was mixed dry with natural clay at the original water content.

3.2. EIS and mCPT samples

In this study, the EIS and mCPT were carried out on cylindrical samples of 50 mm diameter and 20 mm height, as specified in Table 2. The samples were mixed and cast in teflon rings sealed with end caps and cured at 20 °C. This sealed condition was adopted to replicate the low-moisture environment observed in field-mixed samples from Central Station, Gothenburg, where excavated stabilised blocks were found to be devoid of free pore water based on micro-CT observations (Wong et al. 2024). By reproducing similar sealed conditions in the laboratory, the study aims to capture the influence of restricted moisture availability on hydration, microstructural evolution, and strength development.

Table 2. Overview of dimensions of samples prepared.

Test	Dimensions of sample	Batch description	Specifications
EIS, mCPT	50 mm × 20 mm ($D \times H$)	1	Mixed and cast in plastic rings with end caps
nano-CT	280 μm (D)	2	Cored into capillaries from master samples
UCS*	50 mm × 100 mm ($D \times H$)	3	Homogenised and compacted in layers into plastic tubes. Cured in a water bath under a stress of 50 kPa.

Note: mCPT, miniature cone penetration tests; EIS, electrochemical impedance spectroscopy. *The UCS tests are presented in Appendix A.

Fig. 4. Selection of binder mixes for electrochemical impedance spectroscopy (EIS) and miniature cone penetration tests (mCPT). Red circles indicate samples scanned using nano-CT.

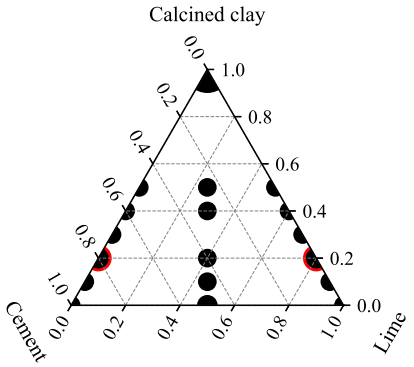

3.3. nano-CT samples

A master batch of the required mixes was prepared from which the miniature samples were cored into quartz capillaries (Hilgenberg GmbH Prod. No. 4017503), with a diameter of 300 μm and a wall thickness of 10 μm. The capillaries were sealed with grease and Loctite super glue to avoid drying due to contact with air and cured for 56 days at room temperature (20 °C). A similar sealed condition as EIS and mCPT samples was used to maintain a low-moisture environment, consistent with field conditions (Wong et al. 2024).

A summary of the different sample preparation methods for each technique, together with the dimensions of the samples in detail, is presented in Table 2.

4. Experimental programme

The binder mixes studied using the tests above are represented in Fig. 4. The black dots denote the mixes chosen to perform EIS and mCPT, and the red circles indicate the mixes chosen to perform nano-CT.

A detailed description of the experimental campaign is given in Table 3. The mix identities follow the format LX_CX_CCY, where L represents lime, C represents cement, and CC stands for calcined clay. The values X and Y indicate the percentage of each component in the binder, where Y is the percentage of replaced CC. For example, L80_CC20 refers to a binder with 80% lime and 20% calcined clay, while L25_C25_CC50 represents a mix containing 25% lime, 25% cement, and 50% calcined clay.

EIS was performed at 7, 14, 28, 36, and 56 days of curing and mCPT was performed on the same samples at the end of 56 days of curing. The design of the mixes enables the investigation of the variation of three components: lime, cement, and calcined clay, limiting the maximum replacement of binders with calcined clay to 50%.

The reaction mechanisms differ depending on whether the mixes are cement-based, lime-based, or a combination of both, which are referred to as the control binders. The effect of lime and cement control binders on the emerging microstructure in the optimum mix was also assessed with nano-CT. This method investigated the percentage of pores and the unhydrated fraction in the mixes with different control binders after 56 days.

Figure 5 shows a schematic overview of the methods used, sample sizes, and length scales accessed by the tests. mCPT and EIS were used as methods to screen a large number of samples with varying mixes, aiming to identify optimal formulations with mechanical properties comparable to the traditional lime–cement mix. The selected mixes were then subjected to further analysis to investigate their microstructural characteristics, including the porosity and the unhydrated fraction. Although both EIS and nano-CT allow for the determination of properties related to the hydration process at the material scale (sub-micron), EIS is a bulk measurement for large samples, while the nano-CT requires miniature samples yielding 3D spatial information. On the other hand, mCPT tests allow for the determination of engineering parameters such as strength in the laboratory scale (deci-meter), on samples with a sample size comparable to that of EIS.

5. Results

5.1. EIS

The evolution of R_s as a function of curing time with control binders L (lime), C (cement), and LC (lime–cement), when replaced with different proportions of calcined clay (CC), is shown in Figs. 6*a*, 6*b*, and 6*c*. Error bars represent the minimum and maximum values.

For L-control binders, a bilinear increase in bulk resistance R_s is observed over the curing time, as shown in Fig. 6*a*. The increase in R_s with time was slow until 28 days of curing, while after 28 days the increase in R_s was approximately three times faster. The R_s values for L-control samples with 10% (L90_CC10) and 20% (L80_CC20) replacement with calcined clay resulted in greater resistance compared to the pure lime-based mix (L_100), suggesting a lower capillary porosity and controlled hydration in mix L80_CC20.

For C-control mixes, R_s increased four times in a span of 49 days, as shown in Fig. 6*b*. The increase in R_s for all mixes was

Table 3. Overview of test plan.

Mix	Binders (%)			Batch	Time of curing (days)				
	Lime	Cement	Calcined clay		7	14	28	36	56
L_100	100	0	0	1	EIS	EIS	EIS	EIS	EIS, mCPT
L90_CC10	90	0	10	1	EIS	EIS	EIS	EIS	EIS, mCPT
L80_CC20	80	0	20	1,2,3	EIS, mCPT, UCS*	EIS, mCPT, UCS*	EIS, mCPT, UCS*	EIS	EIS, mCPT, nano-CT
L70_CC30	70	0	30	1	EIS	EIS	EIS	EIS	EIS, mCPT
L60_CC40	60	0	40	1	EIS	EIS	EIS	EIS	EIS, mCPT
L50_CC50	50	0	50	1	EIS	EIS	EIS	EIS	EIS, mCPT
C_100	0	100	0	1	EIS	EIS	EIS	EIS	EIS, mCPT
C90_CC10	0	90	10	1	EIS	EIS	EIS	EIS	EIS, mCPT
C80_CC20	0	80	20	1,2	EIS	EIS	EIS	EIS	EIS, mCPT, nano-CT
C70_CC30	0	70	30	1	EIS	EIS	EIS	EIS	EIS, mCPT
C60_CC40	0	60	40	1	EIS	EIS	EIS	EIS	EIS, mCPT
C50_CC50	0	50	50	1	EIS	EIS	EIS	EIS	EIS, mCPT
L50_C50	50	50	0	1,2,3	EIS, mCPT	EIS, mCPT, UCS*	EIS, mCPT, UCS*	EIS	EIS, mCPT
L45_C45_CC10	45	45	10	1	EIS	EIS	EIS	EIS	EIS, mCPT
L40_C40_CC20	40	40	20	1	EIS	EIS	EIS	EIS	EIS, mCPT
L30_C30_CC40	30	30	40	1	EIS	EIS	EIS	EIS	EIS, mCPT
L25_C25_CC50	25	25	50	1	EIS	EIS	EIS	EIS	EIS, mCPT
CC_100	0	0	100	1	–	–	–	–	EIS, mCPT

Note: mCPT, miniature cone penetration tests; EIS, electrochemical impedance spectroscopy.*The results of the UCS tests are presented in Appendix A.

Fig. 5. Schematic representation of the methods used and the length scales involved.

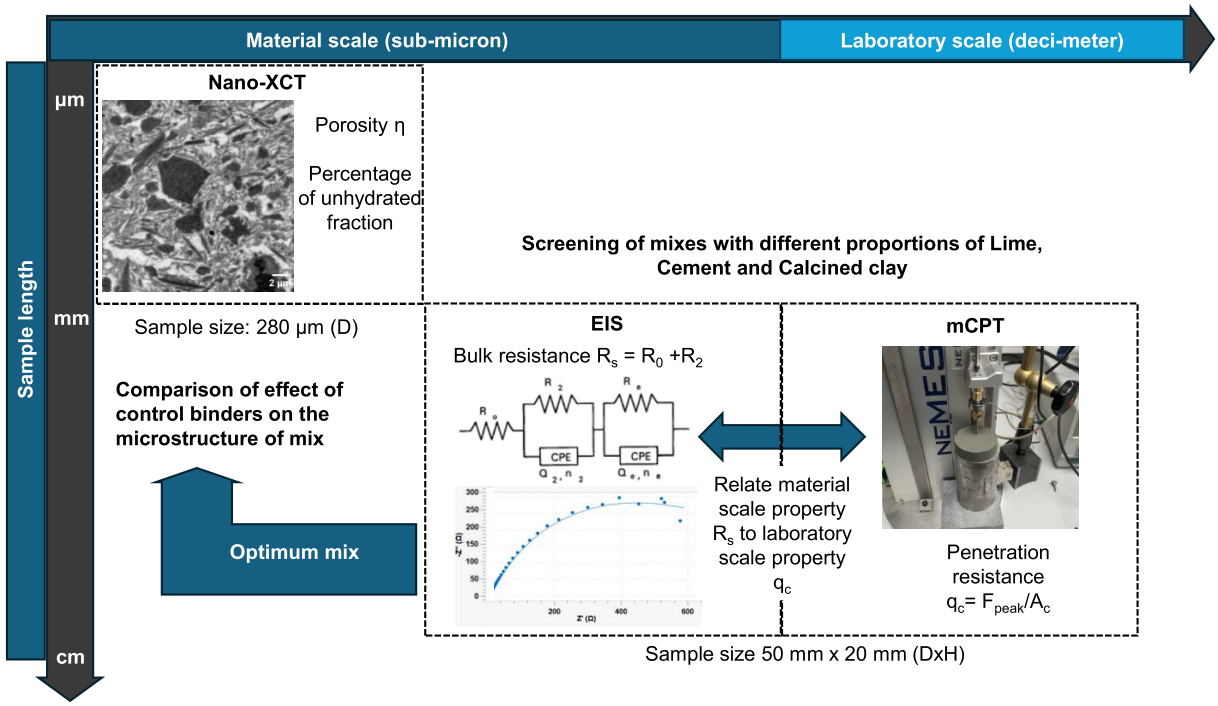

mostly linear before reaching 36 days. After 36 days, the increase in the resistance was seen to be nearly 50% slower. The latter suggests that after 36 days the depletion of pore water, as well as the formation of cementation products, causes disconnected capillary pores, leading to a slower increase in the bulk resistance.

The slower curing in the L-control mixes compared to the C-control mixes cannot be completely attributed to the typical late reaction of calcined clays, since highly reactive calcined kaolinites are used as SCM in the binders considered. A possible explanation for the delayed response is the slower reaction of the sensitive clay with lime than with cement (e.g., Åhnberg and Johansson 2005), as well as the dispersion of the calcined clay causing differences in reactivity. Finally, in cement-containing systems, the lack of water for the hydration of cement is another contributing factor.

Fig. 6. Evolution of bulk resistance R_s for different control mixes at 7, 14, 28, 36, and 56 days of curing. Here, L—lime, C—cement, and CC—calcined clay.

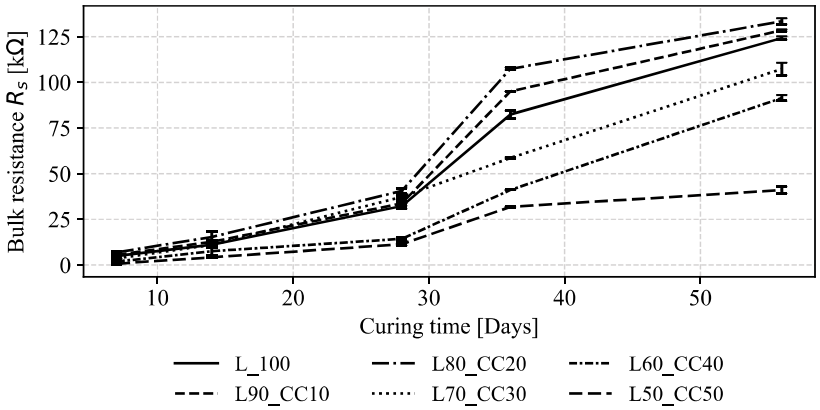

(a) Lime control mixes

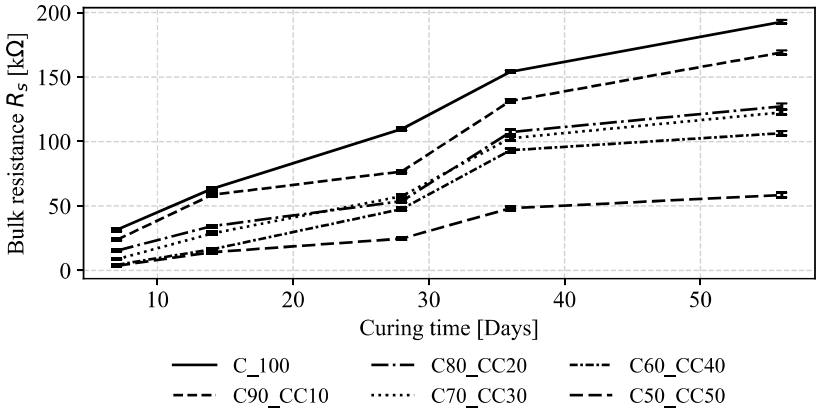

(b) Cement control mixes

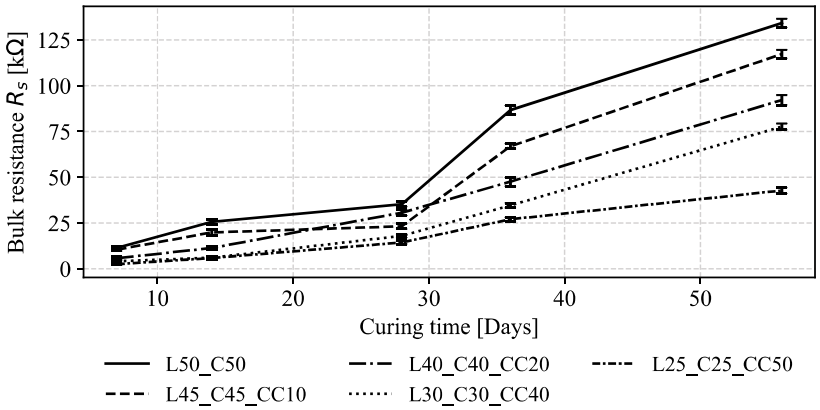

(c) Lime–cement control mixes

The LC-control mixes shown in Fig. 6*c* showed a trend in the resistance R_s similar to that observed in the C-control mixes. This indicates that the presence of cement in these mixes significantly influenced the dominant reaction mechanisms.

Figure 7*a* summarises R_s at 56 days for lime, cement, and lime–cement control samples, respectively, as a function of the percentage of binders replaced with calcined clay. Figure 7*b* shows the same results showing R_s at 56 days of curing on the ternary diagram (varying proportions of lime, cement, and calcined clay). Figure 7*a* shows that, for cement control mixes, R_s dropped by approximately 25 kΩ for every 10% of binder replaced by CC in the C-control mixes. The resistance R_s measured in the LC-control mixes, however, was approximately 10% lower at 56 days than the resistance R_s obtained in the C-control mixes containing the same amount of CC replacement. The lower R_s in the LC-control mix suggests that the rapid hydration of cement consumes most of the available pore water, leaving insufficient water for the

Fig. 7. Bulk resistance R_s at the end of 56 days. Here, L—lime, C—cement, LC—lime–cement (50:50).

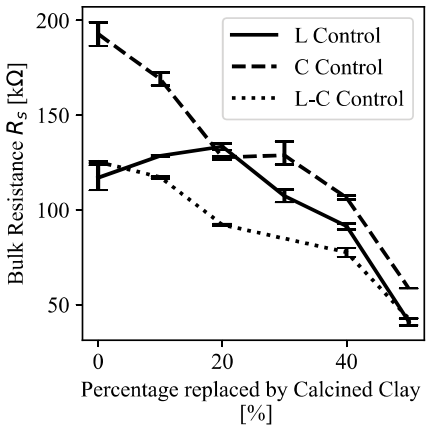

(a) R_s vs. Percentage replaced with calcined clay at 56 days (with error bars).

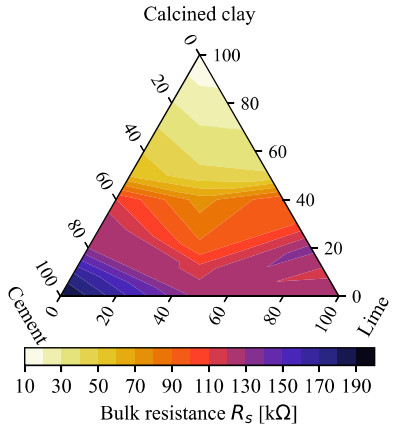

(b) Ternary diagram of bulk resistance R_s at 56 days.

Fig. 8. Normalised R_s versus percentage replaced with calcined clay (with error bars). Here, L—lime, C—cement, LC—lime–cement (50:50).

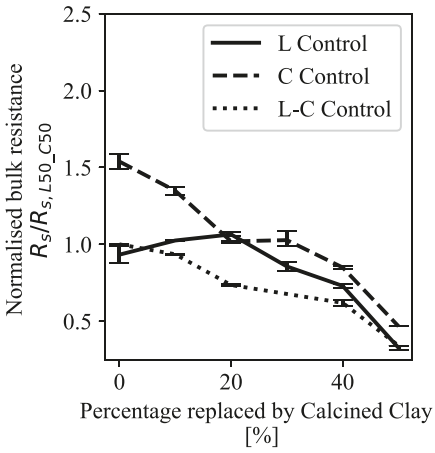

slower hydrating lime, thus limiting the contribution of lime to the formation of hydration products.

For the L-control samples, a nonlinear trend in R_s is observed with increasing calcined clay content, where R_s increases up to 20% replacement and then begins to decline. This suggests the presence of optimal lime content in mix L80_CC20, resulting in increased formation of hydration products that reduce the capillary porosity, while limiting excess unreacted lime in the mix when compared to the mixes having a larger amount of lime i.e., mixes L90_CC10 and L_100.

Figure 8 depicts R_s plotted in Fig. 7*a* normalised with respect to the R_s values obtained for the traditionally employed mix L50_C50, $R_{s,L50\_C50}$ at 56 days of curing. Based on Fig. 8, it is evident that for L-control samples, the maximum replacement that resulted in a normalised resistance value at least comparable to $R_{s,L50\_C50}$ ($R_s/R_{s,L50\_C50} \geq 1$) was mix L80_CC20. In the case of the C-control samples, the maximum replacement could go up to 30%. For the LC-control samples, normalised R_s remained consistently below 1 at all levels of calcined clay replacement, indicating that the incorporation of calcined clay in these mixes did not lead to an enhancement in the microstructural properties compared to the traditionally used mix. Based on the highest amount of binder replacement that resulted in a normalised resistance value $q_{c,\text{peak}}/q_{c,} \geq 1$, the L-control mix with 20% replacement (L80_CC20), and the C-control mix with 20% replacement (C80_CC20) were selected as the optimal formulations for further investigation. Although the C-control mix could accommodate up to 30% replacement while still meeting the resistance threshold, a 20% replacement level was chosen for both systems to enable a consistent comparison of the control binders.

5.2. mCPT

The results of $q_{c,\text{ peak}}$ from mCPT at 56 days of curing are plotted in Fig. 9*a* with error bars indicating the minimum and maximum values. The observed variability is attributed to the heterogeneous nature of stabilised clays and the mixing process, associated with nonuniform binder distribution and local variations in hydration. The penetration resistance values $q_{c,\text{ peak}}$ at 56 days of curing are also plotted for varying proportions of lime, cement, and calcined clay in Fig. 9*b*, presented as a ternary plot.

For C-control mixes, the resulting $q_{c,\text{ peak}}$ followed a linear trend: as the amount of replacement with CC increased, $q_{c,\text{ peak}}$ decreased almost linearly. For every 10% replacement of CC, the penetration resistance decreased by approximately 2 MPa.

When LC-control mixes were compared with C-control mixes, the behaviour of the LC-control mixes resembled that of the C-control mixes. However, the cone penetration resistance $q_{c,\text{ peak}}$ measured in the LC-control mixes was 4 MPa lower than that of the C-control mixes when the same amount of binder was replaced with calcined clay.

In L-control mixes, the resulting $q_{c,\text{ peak}}$ increased linearly to 20% replacement with calcined clay, similar to the results

Fig. 9. Penetration resistance $q_{c,\,peak}$ (4 mm penetration depth) at the end of 56 days. Here, L—lime, C—cement, LC—lime–cement (50:50).

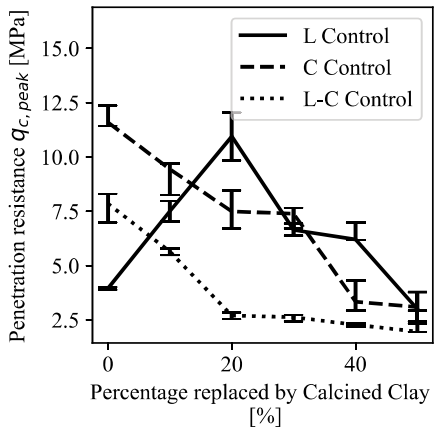

(a) $q_{c,peak}$ vs Percentage replaced with calcined clay at 56 days (with error bars).

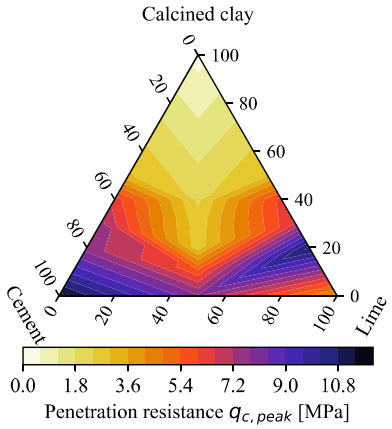

(b) Ternary diagram of penetration resistance $q_{c,peak}$ at 56 days.

Fig. 10. Normalised $q_{c,\,peak}$ versus percentage replaced with calcined clay (with error bars) at the end of 56 days. Here, L—lime, C—cement, LC—lime–cement (50:50).

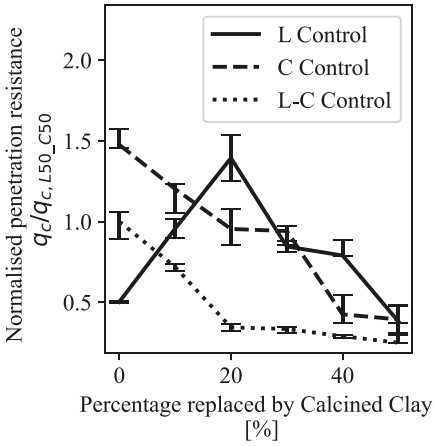

Fig. 11. Penetration resistance $q_{c,\,peak}$ at 7, 14, 28, and 56 days (with error bars) for L80_CC20 and L50_C50.

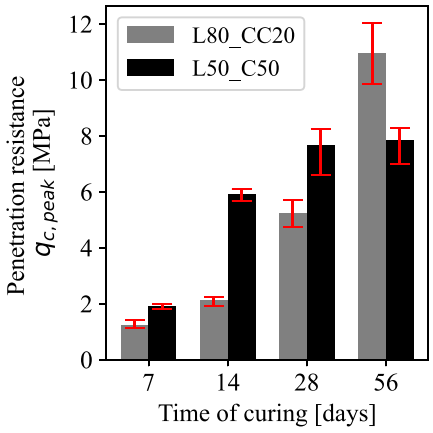

obtained from EIS. As the replacement of calcined clay increases beyond this amount, $q_{c,\,peak}$ decreased by approximately 3 MPa for every 10% lime replaced with calcined clay.

Figure 10 depicts the $q_{c,\,peak}$ plotted in Fig. 9*a* normalised with respect to the $q_{c,\,peak}$ obtained for the traditionally employed mix L50_C50, $q_{c,L50\_C50}$, at 56 days of curing. Similarly to the electrical bulk resistance, Figure 10 shows that for the L-control and C-control samples, the maximum replacement that resulted in a normalised resistance value $q_{c,peak}/q_{c,} \geq 1$ was 20% and 30%. Based on these results and the results from EIS, the mix, L80_CC20, was selected for comparison with the traditional lime–cement mix L50_C50 at 7, 14, 28, and 56 days (Fig. 11).

For mix L80_CC20, $q_{c,\,peak}$ increased by 1 MPa between 7 and 14 days of curing, 4 MPa between 14 and 28 days of curing, and 6 MPa between 28 and 56 days of curing. For the L50_C50 mix, the increase in $q_{c,\,peak}$ was approximately 3 MPa between days 7 and 14 and 2 MPa between days 14 and 28, while remaining approximately constant between days 28 and 56. The $q_{c,\,peak}$ of the L80_CC20 mix was determined to be 4 MPa lower than mix L50_C50 at 14 days, while at 28 days the difference in the $q_{c,\,peak}$ was determined to be 2 MPa. The resistance $q_{c,\,peak}$ determined for mix L80_CC20 at 28 days lagged behind by 26% when compared with the 28-day $q_{c,\,peak}$ for mix L50_C50. However, the L80_CC20 mix surpassed the $q_{c,\,peak}$ determined for mix L50_C50 by 4 MPa at 56 days. This delayed strength gain in L80_CC20 is attributed to the gradual dissolution of aluminosilicates in the clay by lime, whereas the early strength development in L50_C50 is driven by the high heat of hydration.

5.3. Image analysis

Based on the results of the mCPT and EIS tests, the optimal mixes, L80_CC20 and C80_CC20, were selected for a 3D

morphological analysis at the microscopic scale and scanned using nano-CT.

5.3.1. Phase identification

Figures 12*a* and 12*b* depict a horizontal slice of the 3D reconstructed data set for mixes L80_CC20 and C80_CC20. The data are binned and a normalised greyscale colour map is used. Figures 12*c* and 12*d* show the normalised grey level histograms that correspond to this data. From these histograms, it was possible to differentiate three phases in each image corresponding to (i) the macro-porosity (in red), (ii) the clay matrix in the natural clay (in dark grey), and (iii) the fraction including hydrated calcined clay, CSH, silt particles in the natural clay and unhydrated fraction of lime/cement (in black).

Based on the above distinct histogram regions, the phase repartition in the grayscale images is shown in Figs. 12*e* and 12*f*, following the same colour coding as in the histograms. Additionally, by visual examination, it was possible to further distinguish the unhydrated binder (in light brown) from the hydrated binder (CSH + hydrated calcined clay) and silt fraction (in black), as shown in Figs. 12*e* and 12*f* for the mixes L80_CC20 and C80_CC20, respectively.

The unhydrated binder grains were clearly identifiable in the images as dark regions due to the low X-ray attenuation of calcium-rich materials. These grains are typically surrounded by a layer of calcium–silicate–hydrate (CSH) gel, the product of hydration (Taylor et al. 1997). This hydrated phase was seen to have grey levels similar to that of the silt fraction in the natural clay, making it challenging to resolve distinctly. This combination of phases (CSH + hydrated CC and silt) is highlighted in black in Figs. 12*e* and 12*f*. Note that from Figs. 12*e* and 12*f*, it was not possible to identify micro-pores as the pixel size of the scans did not allow the individual natural clay platelets to be resolved. Consequently, the grey region in Figs. 12*e* and 12*f* is referred to as clay matrix, including the natural clay particles, as well as the micro-pores. The corresponding 3D phase distribution of the mixes L80_CC20 and C80_CC20 is as shown in Fig. 13.

5.3.2. Determination of macro-porosity and unhydrated fraction

Thanks to the phase identification above, it is possible to quantify the macro-porosity of the two mixes by computing the ratio between the volume of the red region in Figs. 12*e* and 12*f*, and the total size of the analysed cropped subvolume. The porosities for mixes L80_CC20 and C80_CC20 were determined to be 23% and 25%, respectively, as summarised in Table 4.

Similarly, the unhydrated binder content was calculated from the volume fraction of the corresponding thresholded phase relative to the total analysed volume, by manually finding the grey level thresholds that isolate the unhydrated lime (light brown region in Figs. 12*e* and 12*f*). The binarised images of the isolated unhydrated binder phase, after applying the selected grey level histogram thresholds, are shown in Figs. 14*a* and 14*b* for the mixes C80_CC20 and L80_CC20, respectively, along with the corresponding vertical cross-sections of the grey-scale images.

For mix L80_CC20, a grey level threshold of $\leq$0.29 was applied to isolate the range of unhydrated lime fraction, while for mix C80_CC20, a grey level threshold of 0.33 was applied to determine the range of the unhydrated cement fraction. The unhydrated volume fraction for the mix C80_CC20 was determined to be 4.05%, while for mix L80_CC20 it was 1.77%, as summarised in Table 4.

A difference of approximately 2% (23% and 25%) in porosity and 2.3% (1.77% and 4.05%) in the unhydrated fraction is observed for the different control binder (lime or cement), while the mixed quantities remain the same. In these samples, the macro-porosity is directly influenced by the pore fluid consumption of the binders, whereas a lower unhydrated fraction corresponds to the formation of a greater amount of cementation products. The lime-rich composite retains a lower proportion of unhydrated binder compared to the cement-rich mix, resulting in increased cementation products and consequently, lower macro-porosity of the sample. This observation is further supported by the EIS and mCPT results.

6. Discussion

This study provides a comprehensive analysis of the replacement of conventional binders used in stabilising natural clays with calcined clay, focussing on the electrochemical, mechanical, and morphological properties of the mixture, while validating the results through cross-scale comparisons. Within this framework, the bulk electrochemical response, governed by the evolution of hydration products and pore structure refinement, serves as a key parameter linking these different scales. This electrochemical response can be directly related to the mechanical strength of the different mixes obtained from mCPT results and further correlated with porosity and the unhydrated fraction derived from nano-CT analysis. Consequently, it provides a holistic framework for interpreting the behaviour of stabilised clays.

The integration of EIS and mCPT enabled the systematic determination of the optimum mix design that balances the maximum binder replacement with the highest improvements in the engineering properties of stabilised natural clays. Additionally, the evolution of bulk resistance R_s from EIS over 56 days further provided valuable insight into the hydration progress and pore connectivity. This observation was corroborated by the strong correlation observed in the cross-plot between R_s and the peak penetration resistance $q_{c,\,peak}$, confirming the consistent relationship between electrical and mechanical performance.

Additional evidence on the microstructural differences between the control mixes (lime-control or cement-control) was provided through nano-CT measurements. The L-control mix was shown to have lower macro-porosity (23% vs. 25%) and lower unreacted binder content (1.77% vs. 4.05%), when compared to the C-control mix. Based on the results of EIS and mCPT, the R_s values for the mixes L80_CC20 and C80_CC20 were comparable, while the $q_{c,\,peak}$ value of L80_CC20 was 3.5 MPa higher than that of C80_CC20.

Fig. 12. Image analysis of mixes: L80_CC20 and C80_CC20. (*a* and *b*) Grayscale images of L80_CC20 and C80_CC20, respectively. (*c* and *d*) Normalised grayscale histograms depicting pixel intensity distributions for L80_CC20 and C80_CC20. (*e* and *f*) Phase identification maps of mixes L80_CC20 and C80_CC20 mixes.

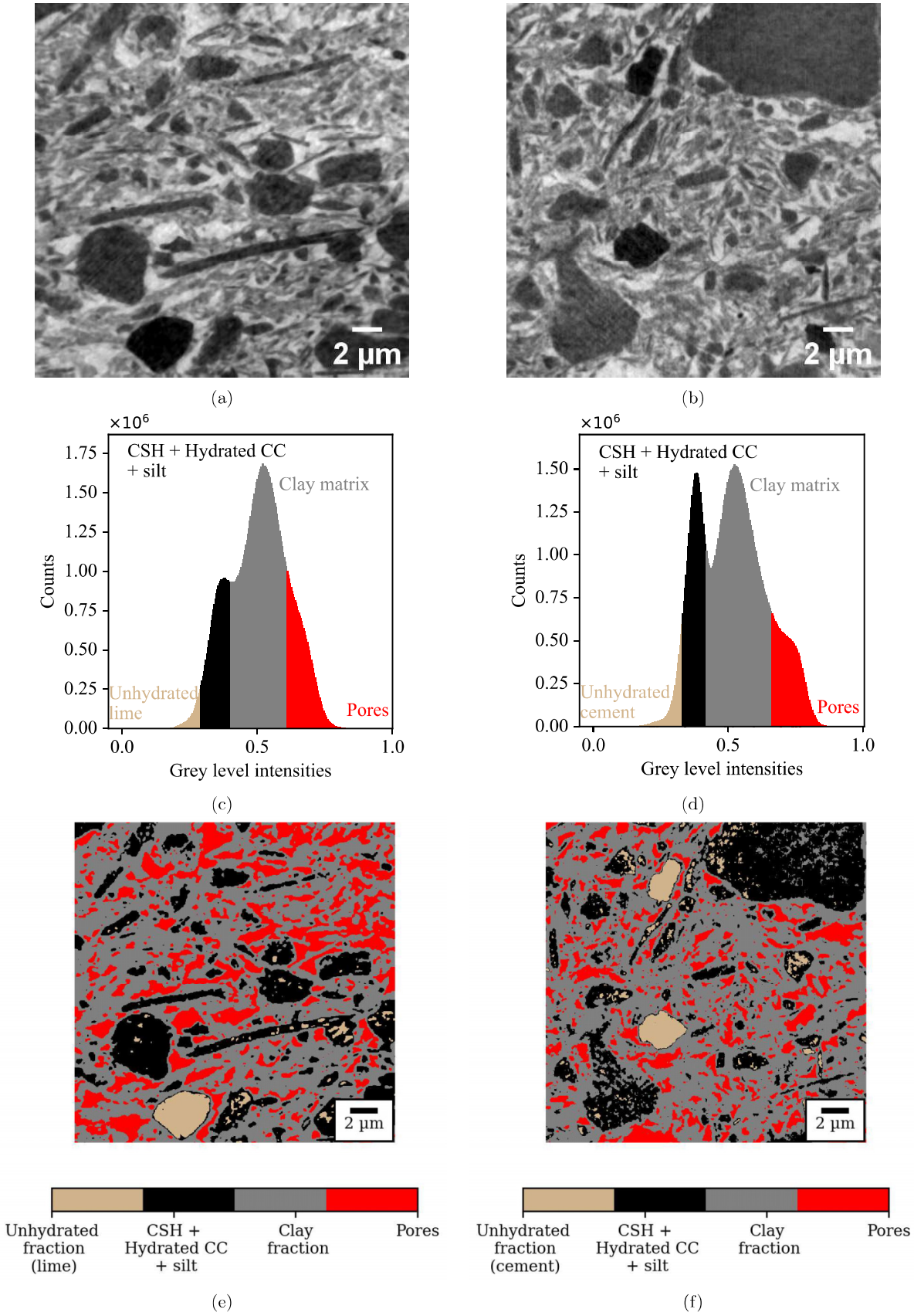

Fig. 13. 3D phase distribution maps of mixes (*a*) L80_CC20 and (*b*) C80_CC20 (dimensions in μm).

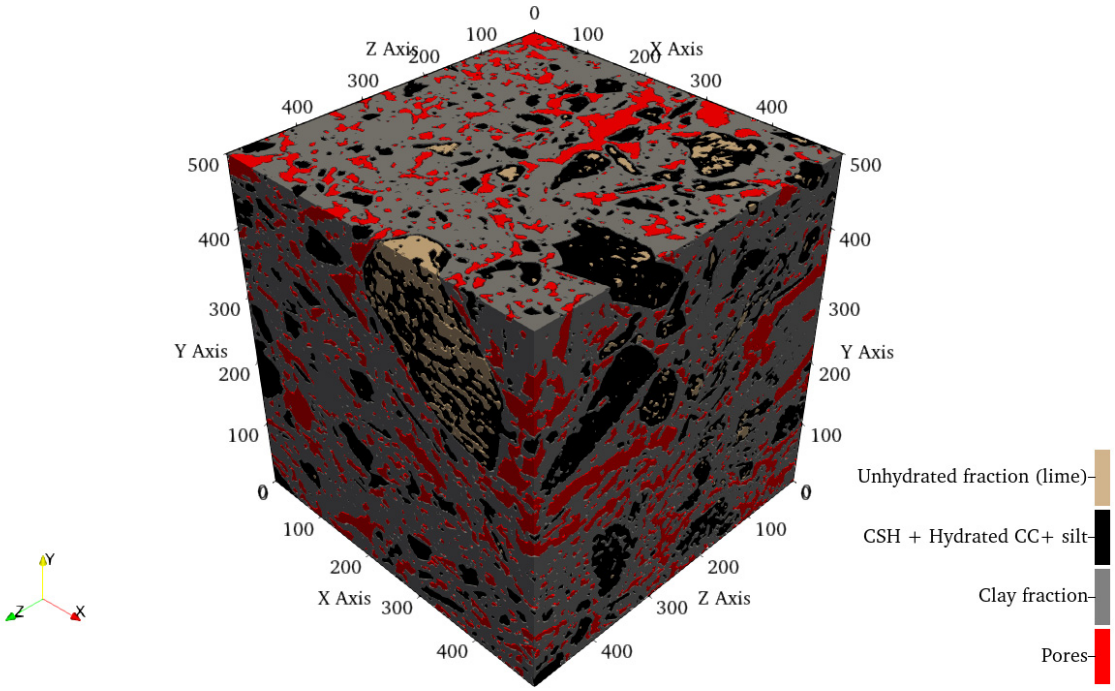

(a) L80_CC20

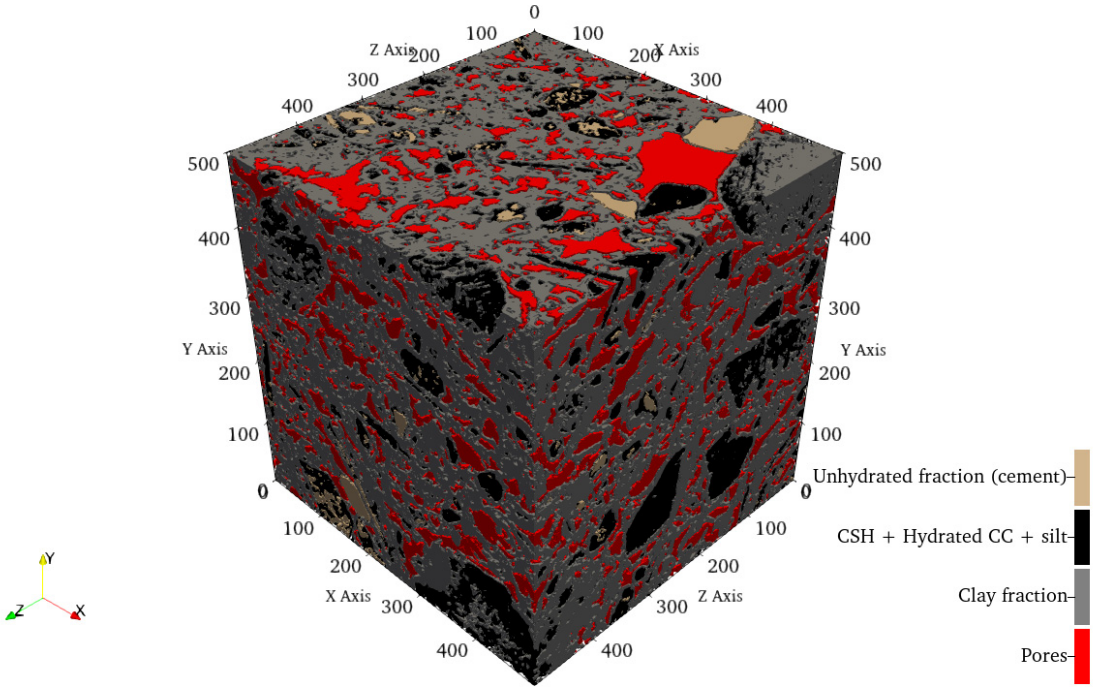

(b) C80_CC20

The similarity in R_s suggests that the pore connectivity and ionic transport characteristics are similar for both mixes. However, the higher cone resistance $q_{c,\,peak}$ observed in L80_CC20 aligns with its reduced porosity and the increased formation of reaction products, which contributes to the increase in density and the mechanical resistance. This is further supported by comparing the differences in unreacted binders. Although a detailed breakdown between reaction products is difficult to achieve with the current image data, where the fraction of reacted calcined clay has grey-level intensities similar to that of the silt in the natural clay matrix, visual inspection strongly suggests that the calcined clay reacted in the alkaline environment created from the lime and/or cement hydration. Similar grey-scale overlap has been

Table 4. Macro-porosity and unhydrated fraction of lime and cement in mixes L80_CC20 and C80_CC20, respectively.

Mix	Macro-porosity		Unhydratd binder fraction	
	Measured (%)	Absolute error (%)	Measured (%)	Absolute error (%)
L80_CC20	23	5.18	1.77	0.89
C80_CC20	25	6.86	4.05	2.34

Fig. 14. Grey level thresholding for unhydrated fraction for mix (*a*) L80_CC20 and (*b*) C80_CC20.

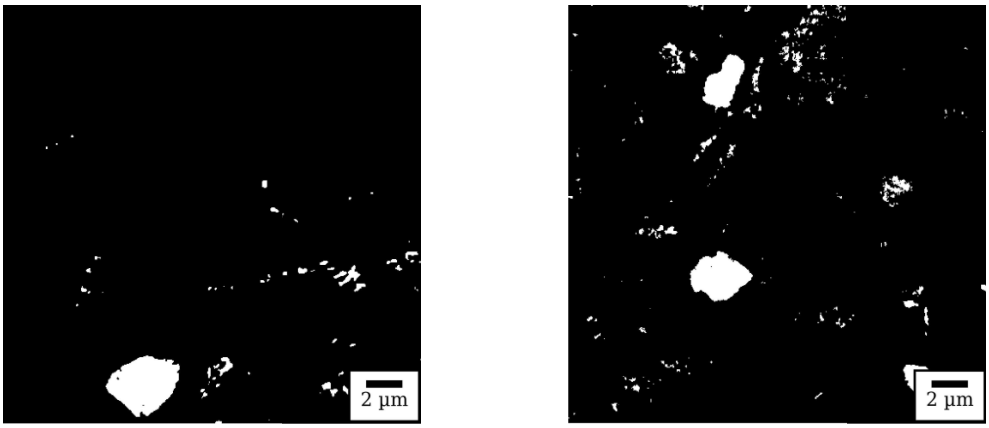

(a) Unhydrated lime phase (b) Unhydrated cement phase

Fig. 15. Bulk resistance R_s versus penetration resistance $q_{c,\,peak}$.

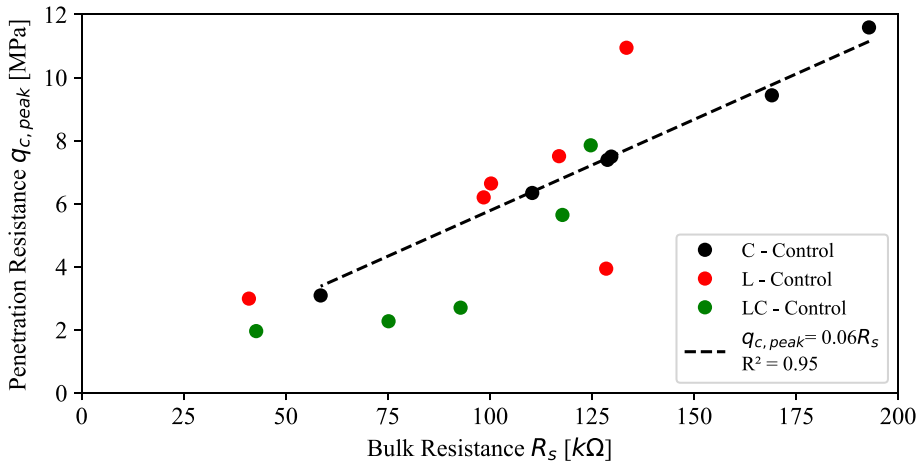

reported in image-based segmentation studies of metakaolin blended cement pastes, motivating the need for further refinement of segmentation approaches (Yu and Geng 2025).

The differences between the cement-based and lime-based mixes studied arise from the higher sensitivity of cement to water availability (Justnes et al. 1996), given that all cement/lime/natural clay-calcined clay systems are highly alkaline and contain sufficient portlandite. A larger fraction of calcined clay in L and C mixes results in a prolonged reaction time, consistent with observations reported for cement pastes containing calcined clays (Siddique and Klaus 2009). In the materials stabilised, the natural clay influences the availability and the flow rate of the water in the pores. Other natural components in the pore water of the natural clay also affect the process. For example, Kärra clay is a marine clay, containing a significant amount of ions (Na^+(0.1875 M), K^+(0.0133 M), Mg^{2+}(0.0068 M), Ca^{2+}(0.0133 M)) that contribute to the stabilisation process. In addition, water availability and transport within the soil–cement matrix play a key role in controlling hydration and pore structure development (Goreham and Lake 2013). Furthermore, a fraction of the natural clay remains unmixed (binder-free), and this further limits the availability of water during the hydration process (Liu et al. 2019). Thus, further investigation of binder amounts and the use of admixtures to enhance reactions during stabilisation of natural clays are needed at both the laboratory and field scales. The results presented in this study indicate a strong correlation between the electrical bulk re-

sistance R_s and the penetration resistance $q_{c,\,peak}$ (strength) for stabilised clays (Fig. 15).

7. Conclusions

The feasibility of using calcined kaolinites as a possible cement replacement to stabilise natural clays has been investigated over a curing period of up to 56 days. In addition to monitoring the process with EIS and mCPT, microstructural changes for a selection of binders have been quantified using X-ray nano-holo-tomography.

The results indicate that the binder, when mixed with natural clays, exhibits behaviour characteristic of supplementary cementitious systems, with slower reaction kinetics and sustained hydration over extended curing periods. The presence and mobility of water in natural clay significantly influences the reaction processes, making cement-based binders particularly sensitive to the amount of calcined clay added.

Finally, under the conditions studied, up to 20% replacement of calcined clays in the lime control sample achieved the mechanical performance comparable to the traditional lime–cement mix commonly used in engineering practice. Based on reported CO_2 emissions for calcined kaolinite (175–420 g/kg CO_2) (Martinez et al. 2023), this level of replacement can reduce total CO_2 emissions by approximately 10%–17%. Further improvements are expected by optimising the total binder content relative to the pore water in the natural clay and by enhancing performance with additional admixtures.

Acknowledgements

We acknowledge the ESRF grant ME-1668 for the beam time at ID16B and support for this series of experiments. Financial support from FORMAS under Grant No. 2021-01340, the Swedish Research Council under Grant No. 2020-03982 and Trafikverket (TRV 2023/29710) is greatly acknowledged. We thank Anders Karlsson for developing the miniature penetration instrument and William Högefjord Kristiansson and Tobias Wedholm for their assistance in performing the UCS tests.

Article information

History dates

Received: 20 January 2026
Accepted: 20 May 2026
Accepted manuscript online: 3 June 2026
Version of record online: 17 July 2026

Copyright

Data availability

Data analysed during this study are available from the corresponding author upon reasonable request.

Author information

Author ORCIDs

Vijayshree Sadasivan https://orcid.org/0009-0000-8763-4863
Jelke Dijkstra https://orcid.org/0000-0003-3792-0727

Author contributions

Conceptualization: VS, AC, AB, JD
Data curation: VS, AC, OS, JV
Formal analysis: VS
Funding acquisition: JD
Investigation: VS, AC, AB, OS, JV, JD
Methodology: VS, AC, AB, JD
Resources: JD
Software: JD
Supervision: AB, JD
Validation: JD
Visualization: VS, AC, AB
Writing – original draft: VS, JD
Writing – review & editing: VS, AC, AB, OS, JV, JD

Competing interests

The authors declare there are no competing interests.

References

Ahmed, A. 2015. Compressive strength and microstructure of soft clay soil stabilized with recycled bassanite. Applied Clay Science, **104**: 27–35. doi:10.1016/j.clay.2014.11.031.

Åhnberg, H., and Johansson, S. 2005. Increase in strength with time in soils stabilised with different types of binder in relation to the type and amount of reaction products. Deep Mixing, **5**: 195–202.

Åhnberg, H., Johansson, S.E., Pihl, H., and Carlsson, T. 2003. Stabilising effects of different binders in some swedish soils. Proceedings of the Institution of Civil Engineers – Ground Improvement, **7**: 9–23.

Andrew, R.M. 2019. Global co$_2$ emissions from cement production, 1928–2018. Earth System Science Data, **11**: 1675–1710. doi:10.5194/essd-11-1675-2019.

Arulrajah, A., Yaghoubi, M., Disfani, M.M., Horpibulsuk, S., Bo, M.W., and Leong, M. 2018. Evaluation of fly ash- and slag-based geopolymers for the improvement of a soft marine clay by deep soil mixing. Soils and Foundatons, **58**: 1358–1370.

ASTM International, 2023. Standard test method for time of setting of concrete mixtures by penetration resistance (ASTM C403/C403M-23). Technical Report. ASTM International, West Conshohocken, PA.

Behnood, A. 2018. Soil and clay stabilization with calcium- and non-calcium-based additives: A state-of-the-art review of challenges, approaches and techniques. Transportation Geotechnics, **17**: 14–32. doi:10.1016/j.trgeo.2018.08.002.

Birmpilis, G., Mohammadi, A.S., Villanova, J., Boller, E., Ando, E., and Dijkstra, J. 2022. Fabric investigation of natural sensitive clay from 3d nano-and microtomography data. Journal of Engineering Mechanics, **148**: 04021151.

Boardman, D.I., Glendinning, S., and Rogers, C.D.F. 2001. Development of stabilisation and solidification in lime–clay mixes. Géotechnique, **51**: 533–543. doi:10.1680/geot.2001.51.6.533.

Casarella, A. 2022. Multi-scale investigation of the thermo-mechanical behaviour of non-active clay.Theses. Université Grenoble Alpes [2020]. Available from https://theses.hal.science/tel-04017761.

Christensen, B., Mason, T., and Jennings, H. 1992. Influence of silica fume on the early hydration of portland cements using impedance spectroscopy. Journal of the American Ceramic Society, **75**: 939–945. doi:10.1111/j.1151-2916.1992.tb04163.x.

Christensen, B.J., Coverdale, T., Olson, R.A., Ford, S.J., Garboczi, E.J., Jennings, H.M., and Mason, T.O. 1994. Impedance spectroscopy of hydrat-

ing cement-based materials: Measurement, interpretation, and application. Journal of the American Ceramic Society, **77**: 2789–2804.

Cloetens, P., Ludwig, W., Baruchel, J., Landuyt, D.V., Guigay, J., and Schlenker, M. 1999. Holotomography: quantitative phase tomography with micrometer resolution using hard synchrotron radiation x–rays. Applied Physics Letters, **75**: 2912–2914. doi:10.1063/1.125225.

Cong, M., Longzhu, C., and Bing, C. 2014. Analysis of strength development in soft clay stabilized with cement-based stabilizer. Construction and Building Materials, **71**: 354–362. doi:10.1016/j.conbuildmat.2014.08.087.

Consoli, N.C., Bittar Marin, E.J., Quiñónez Samaniego, R.A., Scheuermann Filho, H.C., and Cristelo, N.M.C. 2020. Field and laboratory behaviour of fine-grained soil stabilized with lime. Canadian Geotechnical Journal, **57**: 933–938. doi:10.1139/cgj-2019-0271.

Deirieh, A., Chang, I.Y., Whittaker, M.L., Weigand, S., Keane, D., Rix, J., et al. 2018. Particle arrangements in clay slurries: The case against the honeycomb structure. Applied Clay Science, **152**: 166–172.

Durner, W., Iden, S.C., and von Unold, G. 2017. The integral suspension pressure method (isp) for precise particle-size analysis by gravitational sedimentation. Water Resources Research, **53**: 33–48. doi:10.1002/2016WR019830.

Egan, D., and Slocombe, B. 2010. Demonstrating environmental benefits of ground improvement. Proceedings of the Institution of Civil Engineers – Ground Improvement, **163**: 63–69.

Estabragh, A.R., Jahani, A., Javadi, A.A., and Babalar, M. 2022. Assessment of different agents for stabilisation of a clay soil. International Journal of Pavement Engineering, **23**: 160–170. doi:10.1080/10298436.2020.1736293.

Fernandez, R., Martirena, F., and Scrivener, K.L. 2011. The origin of the pozzolanic activity of calcined clay minerals: a comparison between kaolinite, illite and montmorillonite. Cement and Concrete Research, **41**: 113–122.

Froth, H. 2005. Properties of 10-year-old lime-cement columns. In: Proceedings of the International Conference on Deep Mixing: Best Practice and Recent Advances. International Conference on Deep Mixing, Stockholm. pp. 347–351.

Garnier, J., Gaudin, C., Springman, S., Culligan, P., Goodings, D., Konig, D., et al. 2007. Catalogue of scaling laws and similitude questions in geotechnical centrifuge modelling. International Journal of Physical Modelling in Geotechnics, **3**: 1–23. doi:10.13140/2.1.1615.3281.

Goreham, V.C., and Lake, C.B. 2013. Influence of water on diffusion and porosity parameters of soil–cement materials. Canadian Geotechnical Journal, **50**: 351–358. doi:10.1139/cgj-2012-0224.

Hanein, T., Thienel, K.C., Zunino, F., Marsh, A.T.M., Maier, M., Wang, B., et al. 2021. Clay calcination technology: state-of-the-art review by the rilem tc 282-ccl. Materials and Structures, **55**: 3. doi:10.1617/s11527-021-01807-6.

Hazarika, A., Huang, L., and Babaahmadi, A. 2024. Characterisation, activation, and reactivity of heterogenous natural clays. Materials and Structures, **57**: 68. doi:10.1617/s11527-024-02335-9.

Huang, L., Tang, L., Löfgren, I., Olsson, N., and Yang, Z. 2022. Real-time monitoring the electrical properties of pastes to map the hydration induced microstructure change in cement-based materials. Cement and Concrete Composites, **132**: 104639. doi:10.1016/j.cemconcomp.2022.104639.

Jaskulski, R., Jóźwiak-Niedźwiedzka, D., and Yakymechko, Y. 2020. Calcined clay as supplementary cementitious material. Materials (Basel), **13**: 4734.

Jiang, N.J., Du, Y.J., Liu, S.Y., Wei, M.L., Horpibulsuk, S., and Arulrajah, A. 2016. Multi-scale laboratory evaluation of the physical, mechanical, and microstructural properties of soft highway subgrade soil stabilized with calcium carbide residue. Canadian Geotechnical Journal, **53**: 373–383. doi:10.1139/cgj-2015-0245.

Justnes, H., Van Gemert, A., Verboven, F., and Sellevold, E.J. 1996. Total and external chemical shrinkage of low w/c ratio cement pastes. Advances in Cement Research, **8**: 121–126. doi:10.1680/adcr.1996.8.31.121.

Karlsson, M., and Moritz, L. 2014. Trafikverkets tekniska krav för geokonstruktioner TK Geo 13. Swedish Transport Administration, Sweden. Dokument-ID TDOK 2013:0667, Version 1.0, Dokumentdatum 2014-05-01.

Korpa, A., and Trettin, R. 2006. The influence of different drying methods on cement paste microstructures as reflected by gas adsorption: comparison between freeze-drying (f-drying), d-drying, p-drying and oven-drying methods. Cement and Concrete Research, **36**: 634–649. doi:10.1016/j.cemconres.2005.11.021.

Larsson, S., m, M., and Nilsson, B. 2005a. A complementary field study on the uniformity of lime-cement columns for deep mixing. Ground Improvement, **9**: 67–77. doi:10.1680/grim.9.2.67.63640.

Larsson, S., Stille, H., and Olsson, L. 2005b. On horizontal variability in lime-cement columns in deep mixing. Geotechnique, **55**: 33–44. doi:10.1680/geot.2005.55.1.33.

Latifi, N., Rashid, A.S.A., Siddiqua, S., and Horpibulsuk, S. 2015. Microstructural analysis of strength development in low- and high swelling clays stabilized with magnesium chloride solution — a green soil stabilizer. Applied Clay Science, **118**: 195–206. doi:10.1016/j.clay.2015.10.001.

Levita, G., Marchetti, A., Gallone, G., Principigallo, A., and Guerrini, G. 2000. Electrical properties of fluidified portland cement mixes in the early stage of hydration. Cement and Concrete Research, **30**: 923–930. doi:10.1016/S0008-8846(00)00282-9.

Liu, L., Zhou, A., Deng, Y., Cui, Y., Yu, Z., and Yu, C. 2019. Strength performance of cement/slag-based stabilized soft clays. Construction and Building Materials, **211**: 909–918. doi:10.1016/j.conbuildmat.2019.03.256.

Locat, J., Bérubé, M.A., and Choquette, M. 1990. Laboratory investigations on the lime stabilization of sensitive clays: shear strength development. Canadian Geotechnical Journal, **27**: 294–304. doi:10.1139/t90-040.

Martínez-Criado, G., Villanova, J., Tucoulou, R., Salomon, D., Suuronen, J.P., Labouré, S., et al. 2016. ID16B: a hard X-ray nanoprobe beamline at the ESRF for nano-analysis. Journal of Synchrotron Radiation, **23**: 344–352. doi:10.1107/S1600577515019839.

Martinez, D.M., Horvath, A., and Monteiro, P.J. 2023. Comparative environmental assessment of limestone calcined clay cements and typical blended cements. Environmental Research Communications. **5**: 055002.

Mason, T., Campo, M., Hixson, A., and Woo, L. 2002. Impedance spectroscopy of fiber-reinforced cement composites. Cement and Concrete Composites, **24**: 457–465. doi:10.1016/S0958-9465(01)00077-4.

McCarter, W., Chrisp, T., Starrs, G., and Blewett, J. 2003. Characterization and monitoring of cement-based systems using intrinsic electrical property measurements. Cement and Concrete Research, **33**: 197–206. doi:10.1016/S0008-8846(02)00824-4.

McCarter, W., Garvin, S., and Bouzid, N. 1988. Impedance measurements on cement paste. Journal of Material Science Letters, **7**: 1056–1057. doi:10.1007/BF00720825.

Mirone, A., Brun, E., Gouillart, E., Tafforeau, P., and Kieffer, J. 2014. The pyhst2 hybrid distributed code for high speed tomographic reconstruction with iterative reconstruction and a priori knowledge capabilities. Nuclear Instruments and Methods in Physics Research Section B: Beam Interactions with Materials and Atoms, **324**: 41–48. doi:10.1016/j.nimb.2013.09.030.

Moseley, M., and Kirsch, K. 2004. Ground improvement. 2nd ed. CRC Press.

Muchui Mugambi, L., Mujombi, S., Mutai, V., Ratumo Toeri, J., Mwiti Marangu, J., and Valentini, L. 2024. Potential of limestone calcined clay cement (LC3) in soil stabilization for application in roads and pavements construction. Case Studies in Construction Materials, **21**: e03706. doi:10.1016/j.cscm.2024.e03706.

Núñez, V., Lotero, A., Bastos, C.A., and Consoli, N.C. 2025. Controlling of the mechanical behavior of mass-stabilized organic clay with various binders. Geotechnical and Geological Engineering, **43**: 54.

Nunez, V., Lotero, A., Bastos, C.A., Sargent, P., and Consoli, N.C. 2024. Mechanical and microstructure analysis of mass-stabilized organic clay thermally cured using a ternary binder. Acta Geotechnica, **19**: 741–762.

Olsson, J., Miller, S., and Alexander, M. 2023. Near-term pathways for decarbonizing global concrete production. Nature Communications, **14**. doi:10.1038/s41467-023-40302-0.

Paniagua, P., Bache, B.K., Karlsrud, K., and Lund, A.K. 2022. Strength and stiffness of laboratory-mixed specimens of stabilised norwegian clays. Proceedings of the Institution of Civil Engineers - Ground Improvement, **175**: 150–163. doi:10.1680/jgrim.19.00051.

Plusquellec, G., Babaahmadi, A., L'Hopital, E., and Mueller, U. 2021. Activated clays as supplementary cementitious material. Technical Re-

port, 2021:25. RISE Research Institutes of Sweden, Infrastructure and concrete technology.
Ramírez, A.L., and Korkiala-Tanttu, L. 2023. Stabilisation of malmi soft clay with traditional and low-co2 binders. Transportation Geotechnics, **38**: 100920. doi:10.1016/j.trgeo.2022.100920.
Sargent, P., Hughes, P., and Rouainia, M. 2016. A new low carbon cementitious binder for stabilising weak ground conditions through deep soil mixing. Soils and Foundations, **56**: 1021–1034. doi:10.1016/j.sandf.2016.11.007.
Sargent, P., Hughes, P.N., Rouainia, M., and White, M.L. 2013. The use of alkali activated waste binders in enhancing the mechanical properties and durability of soft alluvial soils. Engineering Geology, **152**: 96–108. doi:10.1016/j.enggeo.2012.10.013.
Schindelin, J., Arganda-Carreras, I., Frise, E., Kaynig, V., Longair, M., Pietzsch, T., et al. 2012. Fiji: an open-source platform for biological-image analysis. Nature Methods, **9**: 676–682.
Schorcht, F., Kourti, I., Scalet, B.M., Roudier, S., and Sancho, L.D. 2013. Best available techniques (bat) reference document for the production of cement, lime and magnesium oxide. European Commission Joint Research Centre Institute for Prospective Technological Studies, Luxembourg. p. 506.
Scrivener, K.L., John, V.M., and Gartner, E.M. 2018. Eco-efficient cements: Potential economically viable solutions for a low-co2 cement-based materials industry. Cement and Concrete Research, **114**: 2–26.
Sekhar, D.C., and Nayak, S. 2019. Sem and XRD investigations on lithomargic clay stabilized using granulated blast furnace slag and cement. International Journal of Geotechnical Engineering, **13**: 615–629.
Shirani, S., Cuesta, A., Morales-Cantero, A., Santacruz, I., Diaz, A., Trtik, P., et al. 2023. 4d nanoimaging of early age cement hydration. Nature Communications, **14**. doi:10.1038/s41467-023-38380-1.
Siddique, R., and Klaus, J. 2009. Influence of metakaolin on the properties of mortar and concrete: a review. Applied Clay Science, **43**: 392–400. doi:10.1016/j.clay.2008.11.007.
Simoni, M., Wilkes, M.D., Brown, S., Provis, J.L., Kinoshita, H., and Hanein, T. 2022. Decarbonising the lime industry: State-of-the-art. Renewable and Sustainable Energy Reviews, **168**: 112765. doi:10.1016/j.rser.2022.112765.
Snellings, R., Suraneni, P., and Skibsted, J. 2023. Future and emerging supplementary cementitious materials. Cement and Concrete Research, **171**: 107199.
Song, G. 2000. Equivalent circuit model for ac electrochemical impedance spectroscopy of concrete. Cement and Concrete Research, **30**: 1723–1730. doi:10.1016/S0008-8846(00)00400-2.
Swedish Institute for Standards (SIS), 2018. Geotechnical investigation and testing – laboratory testing of soil – part 7: unconfined compression test (iso 17892-7:2017).
Taylor, H.F., et al. 1997. Cement chemistry. Vol. **2**. Thomas Telford, London.
Tironi, A., Trezza, M.A., Scian, A.N., and Irassar, E.F. 2013. Assessment of pozzolanic activity of different calcined clays. Cement and Concrete Composites, **37**: 319–327. doi:10.1016/j.cemconcomp.2013.01.002.
Topolnicki, M. 2004. In-situ soil mixing. In Ground improvement. Spon Press London, UK. pp. 329–433. doi:10.1201/b13678-13.
Turner, L.K., and Collins, F.G. 2013. Carbon dioxide equivalent (co2-e) emissions: A comparison between geopolymer and opc cement concrete. Construction and Building Materials, **43**: 125–130. doi:10.1016/j.conbuildmat.2013.01.023.
Wang, X., and Xiao, P. 2002. Characterisation of clay sintering process using impedance spectroscopy. Journal of the European Ceramic Society, **22**: 471–478. doi:10.1016/S0955-2219(01)00335-1.
Wong, D.Y.C., Sadasivan, V., Isaksson, J., Karlsson, A., and Dijkstra, J. 2024. Trans-scale spatial variability of lime-cement mixed columns. Construction and Building Materials, **417**: 135394. doi:10.1016/j.conbuildmat.2024.135394.
Xie, S.H., Liu, S.Y., Liu, Z.B., and Du, G.Y. 2012. In situ test on soft marine clays with high clay content improved by bidirectional dry jet mixing method. GeoCongress, 988–995. doi:10.1061/9780784412121.102.
Yi, Y., Zheng, X., Liu, S., and Al-Tabbaa, A. 2015. Comparison of reactive magnesia- and carbide slag-activated ground granulated blastfurnace slag and portland cement for stabilisation of a natural soil. Applied Clay Science, **111**: 21–26. doi:10.1016/j.clay.2015.03.023.
Yu, Y., and Geng, G. 2025. Deep learning methods for phase segmentation in backscattered electron images of cement paste and scm-blended systems. Cement and Concrete Composites, **155**: 105810. doi:10.1016/j.cemconcomp.2024.105810.

Appendix A. Comparison of mCPT and UCS

The cone resistance measured with the miniature cone penetration test is directly related to the (compressive) strength in the cementitious material. In the following, the relation between $q_{c,\ \mathrm{peak}}$ at 4 mm penetration and q_u from more traditional unconfined compression tests is established for the new binder mixes for samples with the age of 7, 14, and 28 days, respectively.

A1. UCS test

The UCS tests were performed using a GDS loading frame that has a stroke of 40 mm and a load cell with capacity 10 kN $\pm$ 10 N. The setup included a pair of extensometers (one on each side of the sample), with a gauge length of 65 mm and a resolution of 10 μm, which aided in measuring the axial strains in the middle third section of the sample height. The tests were conducted on cylindrical specimens in accordance with SS-EN ISO 17892-7:2018 (Swedish Institute for Standards (SIS) 2018). A reduced loading rate of 0.1 mm min^{-1} was used to minimise sudden brittle failure and ensure accurate measurement of the stress–strain response. From these tests, the unconfined compressive strength q_u and the secant Young's modulus at 50% (E_{50}), were determined.

The UCS samples were prepared by homogenising the clays in a rotary mixer for 30 s. After homogenising the clay, the binder mixes in the required proportions were added in three batches with each batch being mixed for 60 s each. This resulted in a total mixing time of 3.5 min. The mixed clay composite was then compacted into plastic tubes of diameter 50 mm and height 250 mm. The top and bottom of the samples were fitted with end caps and porous discs and cured under stress of 50 kPa in a water bath allowing water to flow from the top and bottom. Tests were performed on two samples of approximate dimensions 50 mm $\times$ 100 mm ($D \times H$) extruded from the plastic tube.

A2. UCS results

The results of the peak strength (q_u) and the secant stiffness at 50% failure (E_{50}) are plotted in Fig. A1. The error bars in the bar plots represent the range between the minimum and maximum values. The E_{50} values were obtained as the mean of secant stiffnesses evaluated from the local strain measurements.

A3. Relation between mCPT and UCS

The results q_u from the UCS tests are correlated to the $q_{c,\ \mathrm{peak}}$ results from the miniature penetration tests in Fig. A2. For consistency in comparison, q_u values are plotted in MPa. q_u was determined to be 29.5 $\times$ q_c with an accuracy $R^2 = 0.99$.

Fig. A1. q_u and E_{50} results from UCS tests at 7, 14, and 28 days (with error bars).

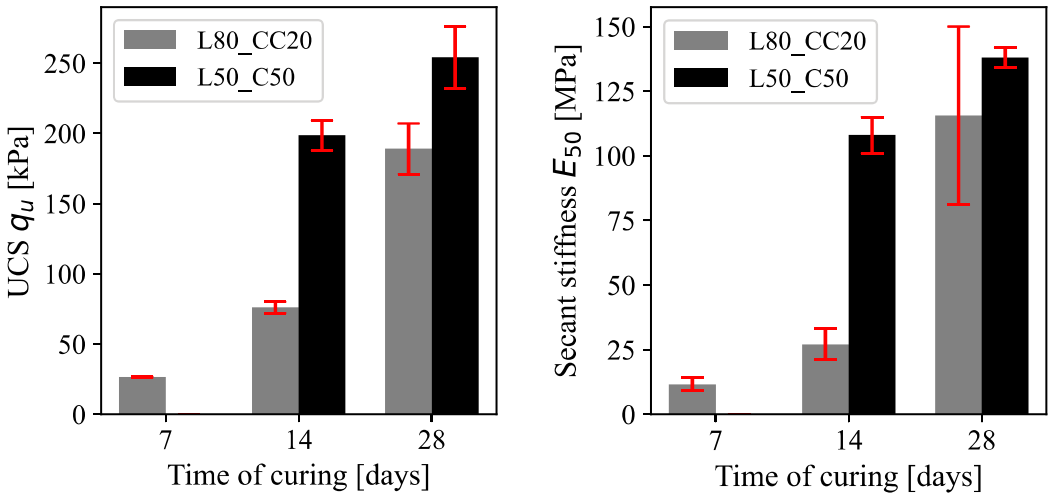

(a) UCS q_u (b) Secant stiffness E_{50}

Fig. A2. UCS q_u versus penetration resistance $q_{c,\,\mathrm{peak}}$ (with error bars).

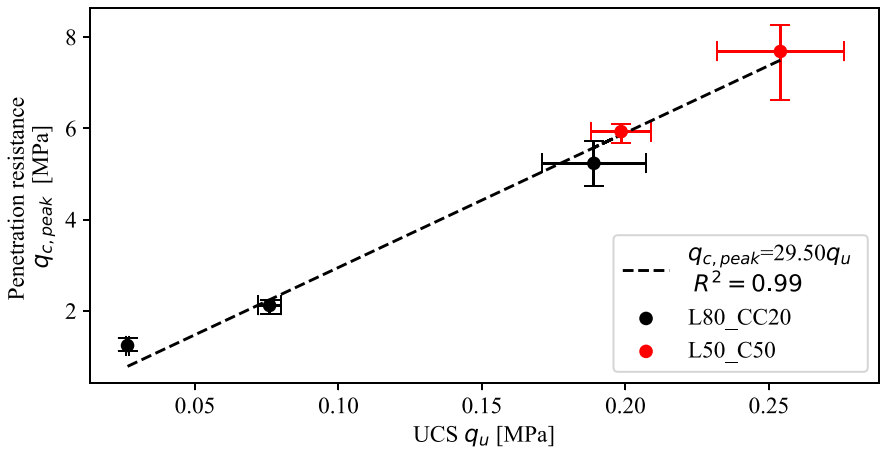

Appendix B. Image pre-processing

Figure B1 shows the mid-slice (x–y plane) of the selected sub-volume before and after filtering and normalisation.

The 3D grey scale images of mixes L80_CC20 and C80_CC20 are shown in Figs. B2*a* and B2*b*, respectively.

Fig. B1. Pre-processing of nano-CT reconstructed images (2× binning). (Left) Before and (right) after noise filtering and histogram normalisation for mix C80_CC20.

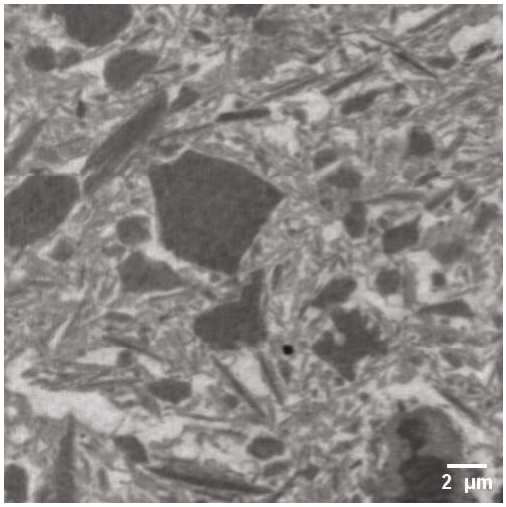

(a) Before.

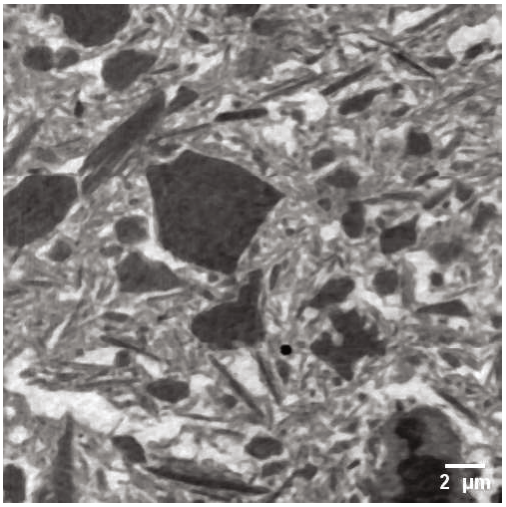

(b) After.

Fig. B2. 3D greyscale images of mixes (*a*) L80_CC20 and (*b*) C80_CC20 (dimensions in μm).

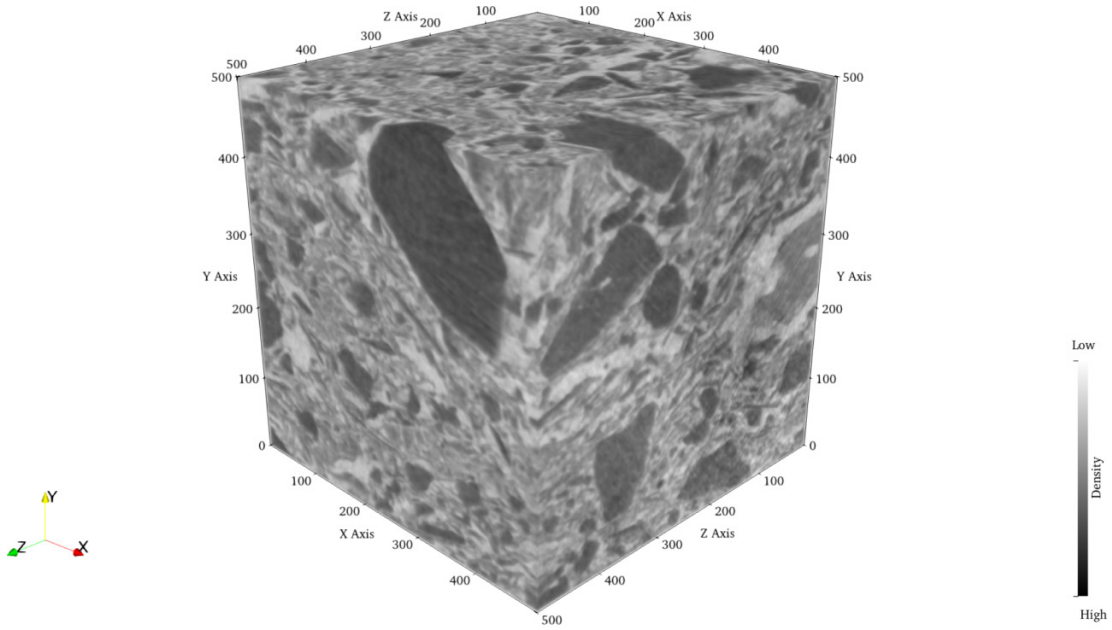

(a) L80_CC20

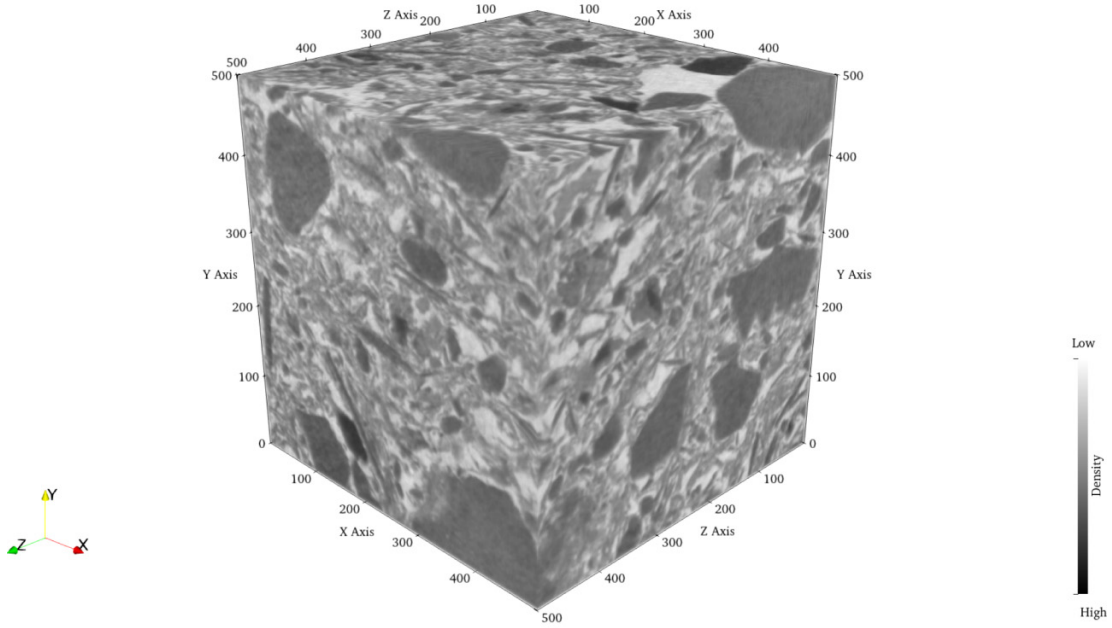

(b) C80_CC20